Static and dynamic stiffness measurements with Opalinus Clay

Serhii Lozovyi[1], Andreas Bauer[1,2]

1 Norwegian University of Science and Technology, Trondheim, Norway

serhii.lozovyi@sintef.no

2 SINTEF Petroleum Research, Trondheim, Norway

AndreasKurtMarcel.Bauer@sintef.no

Corresponding author: Serhii Lozovyi, e-mail: serhii.lozovyi@sintef.no

Keywords

Static and dynamic stiffness, Opalinus clay, velocity dispersion, anisotropy

Abstract

In this work, an experimental study was carried out with the aim of reconciling static and dynamic stiffness of Opalinus Clay. The static and dynamic stiffness of core plugs from a shaly and a sandy facies of Opalinus Clay were characterized at two different stress states. The measurements included undrained quasi-static loading-unloading cycles from which the static stiffness was derived, dynamic stiffness measurement at seismic frequencies (0.5 – 150 Hz), and ultrasonic velocity measurements (500 kHz) probing the dynamic stiffness at ultrasonic frequencies. The experiments were carried out in SINTEF's low-frequency cell. The obtained results demonstrate that the difference between static and dynamic stiffness is due to both dispersion and non-elastic effects: Both the sandy and the shaly facies of Opalinus Clay exhibit large dispersion, i.e. a large frequency dependence of dynamic stiffness and acoustic velocities. Especially the dynamic Young's moduli exhibit very high dispersion; between seismic and ultrasonic frequencies they may change by more than a factor 2. P-wave velocities perpendicular to bedding are by more than 200 m/s higher at ultrasonic frequencies than at seismic frequencies. The static undrained stiffness of both the sandy and the shaly facies is strongly influenced by non-elastic effects, resulting in significant softening during both loading and unloading with increasing stress amplitude. The zero-stress extrapolated static undrained stiffness, however, reflects the purely elastic response and agrees well with the dynamic stiffness at seismic frequency.

1 Introduction

The ability to accurately derive static mechanical rock properties from wave velocities is crucial for building reliable subsurface geomechanical models in cases where there is no or not enough rock material available for direct stiffness and strength measurements. Applications of these geomechanical models include amongst others integrity assessments for subsurface nuclear waste disposal, CO_2 sequestration, as well as oil and gas reservoirs.

Opalinus Clay is considered as host rock for nuclear waste disposal in Switzerland. Long-term storage of high-level nuclear waste will require well-calibrated geomechanical models in order to model stress and strain changes as well as possible rock failure in the host rock formation around the repositories caused by, e.g., temperature and/or gas-pressure changes inside the repositories. Most rocks, including Opalinus Clay, are heterogeneous, and their mechanical properties can vary widely within the same formation. Seismic surveys allow for a three-dimensional mapping of acoustic velocities. Those velocities are related to the dynamic rock stiffness, which is usually higher than the static stiffness needed for geomechanical modeling. Several correlations have been developed in the past that relate static an dynamic stiffness but the reasons for why dynamic and static stiffness are different are still not fully understood (King, 1969; Heerden, 1987; Eissa and Kazi, 1988; Yale and Swami, 2017). For an ideal linear-elastic medium, dynamic and static stiffness are the same. For example, a static mechanical test with an aluminium sample (for small enough stresses to avoid plastic deformation), will give the same stiffness as the dynamic stiffness obtained from ultrasonic wave velocity measurements. Rocks are more complex; they are fluid-saturated porous media, and dynamic and static stiffness are generally not the same. For Opalinus Clay, e.g., the static Young's moduli measured in triaxial compression tests need to be scaled by a factor of two to four to match the dynamic Young's moduli calculated from acoustic wave velocities (Nagra,

2002; Schuster et al., 2017). While acoustic-velocity measurements probe the dynamic undrained stiffness, mechanical tests usually probe the quasi-static drained stiffness. Here, "drained" means that the fluid can leave or enter the rock during compression so that the fluid pressure (pore pressure) remains constant. In an undrained rock deformation, the fluid is confined, and, depending on the compressibility of the fluid, the fluid pressure in the rock will change when stress is applied to the rock. The difference between drained and undrained stiffness is captured by well-established poroelastic models (Detournay and Cheng, 1993; Wang, 2000; Mavko et al., 2009) and not subject of the present study. In the present work, the difference between the dynamic and the static undrained stiffness is investigated.

Several studies have identified non-elastic processes in quasi-static rock testing (stress amplitude effects), and stiffness dispersion (i.e. frequency dependence of the stiffness) as the main causes of the discrepancy between undrained static and dynamic stiffness (e.g. Walsh, 1966; Tutuncu et al., 1998; Fjær, 2009). It has been reported that non-elastic processes can already be activated at strains as low as 10^{-6}, resulting in a reduced stiffness and a deviation from the dynamic, purely elastic stiffness (Winkler et al., 1979; Batzle et al., 2006; Lozovyi et al., 2017). Fjær et al., (2013) have developed a simple model to account for non-elastic processes, which can be used to find the purely elastic stiffness from static compression tests. The model is based on the empirical finding that the rock compressibility increases linearly with stress amplitude.

Some rocks, especially shales, exhibit relatively large stiffness dispersion (Duranti et al., 2005; Hofmann, 2006; Tutuncu, 2010; Szewczyk et al., 2016; Lozovyi et al., 2018). Quasi-static rock deformations in static tests are usually done with loading rates that correspond to average loading rates of dynamic measurements in the sub-Hz frequency regime. Seismic measurements are typically done at frequencies between 1 Hz and 100 Hz, sonic measurements (sonic logging tools) in

the kHz range, and ultrasonic measurements above 100 kHz. In the presence of stiffness/velocity dispersion, the difference between static and dynamic stiffness will depend on the frequency of the dynamic measurements. Numerous pore-scale and meso-scale dispersion mechanisms have been suggested, and several dispersion models have been developed (for an overview, se e.g. Müller et al. (2010). Experimental data, however, is still scarce (Spencer, 1981; Suarez-Rivera et al., 2001; Batzle et al., 2005, 2006; Sarker and Batzle, 2010; Delle Piane et al., 2014). Stiffness/velocity dispersion of shales is still poorly understood. There is no model yet available that could predict stiffness or velocity dispersion of a shale based on the petrophysical and mineralogical properties. Therefore, experimental measurements are needed to quantify the degree of dispersion in shales. Such measurements require custom-made equipment, and there are only a few groups in the world that can do such measurements in the laboratory (Subramaniyan et al., 2014).

In this paper, a comprehensive laboratory investigation was carried out in order to understand and quantify the relation between static and dynamic elastic properties in Opalinus Clay. A study of the frequency dependence of dynamic moduli along with systematic static measurements at controlled stress conditions gave insights in the static-dynamic properties of Opalinus Clay. Two different facies of Opalinus Clay, a shaly and a sandy facies, were investigated. The measurements were carried out with core plugs using SINTEF's low-frequency cell (Szewczyk et al., 2016), and include quasi-static undrained loading/unloading cycles, dynamic-stiffness measurements at seismic frequencies, and ultrasonic measurements. The tested core plugs were drilled from cores taken in September 2016 during a dedicated scientific drilling operation (BGC-1) at the Mont Terri underground laboratory. A 32 m-deep hole was drilled from gallery 08 into the surrounding Opalinus Clay formation with the hole axis perpendicular to the bedding planes.

2 Experimental details and data analysis

2.1 Sample preparation and preservation

Both a sandy and a shaly facies of Opalinus Clay were studied in this work. Selected sections of a core taken from the BGC-1 borehole at the Mont Terri underground laboratory were preserved and shipped to SINTEF. Based on CT scans and photographs of the cores, zones without visible cracks and prominent inhomogeneities were identified. From these zones, several sets of cylindrical core plugs were drilled out with 0°, 45°, and 90° orientation to the bedding planes.

Opalinus Clay of Mont Terri is an overconsolidated shale that was formed as a marine sediment consisting mainly of silicates, carbonates and quartz (Bossart, 2011). The difference between sandy and shaly facies is mainly in grain size distribution and quartz/clay content. The shaly facies is dominated by the silt and clay fractions (10% of sand, 57% of silt and 33% of clay), whereas the sandy facies shows higher values for the coarser fractions (11% of gravel, 29% of sand, 42% of silt and 18% of clay) (Minardi et al., 2017). Mineralogical composition of the tested in this study core samples is shown in Table 1. The first digit in sample numbering, 1, 2, 3, or 4, indicates a set number. Each set consists of three samples with different orientations (0°, 45°, and 90°). The sandy facies have nearly equal distribution of quartz and clay, whereas shaly facies is dominated by clay minerals. Note that the set #1 is rather heterogeneous, resulting in some inconsistent results, as described later in the paper.

An average density of the tested samples is 2.49 g/cm^2 for sandy facies and 2.45 g/cm^2 for shaly facies. The average water content measured after drying the samples in an oven at 105°C is 4.4 wt% for the sandy facies and 6.1 wt% for the shaly facies. Corresponding porosities are 12% and 16% for sandy and shaly facies respectively.

The core plugs with a diameter of 25.4 mm and a nominal length of 50.8 mm were drilled and trimmed with oil. Afterwards, the cores were placed in a desiccator with a relative humidity (RH) of ≈ 93% (using a KNO_3-saturated solution). The procedure of maintaining/re-establishing in-situ saturation conditions is according to (Ewy, 2015; Giger, 2016).

The core plugs were kept in the desiccator for more than 2 weeks before tests. As seen in Figure 1, the weight of the core plugs did not change much during their time in the desiccators. When mounting a core plug into the low-frequency cell (applying strain gages, jacketing, etc.), the core plugs ware exposed to air for less than one hour (with most of the surface covered in first 10-20 minutes).

In the beginning of test, the core plugs were exposed to synthetic brine, when confining stress reached 4 MPa. The following brine composition was used (adopted recipe from Pearson and Waber (2006):

- NaCl: 7.57 g/L H2O
- KCl: 0.10 g/L H2O
- MgCl2: 1.08 g/L H2O
- CaCl2: 0.96 g/L H2O
- Na2SO4: 1.25 g/L H2O

The core-plug densities were obtained from the sample dimensions (diameter, length) and weight measured after the plug was taken out of the desiccator. These densities were taken when calculating velocities from the respective moduli. In fact, the density change as result of loading should be taken into account, but this effect is rather small. Therefore, it is ignored in velocity calculus and included in estimated systematic error of the measurement instead.

2.2 The low-frequency apparatus

The low-frequency apparatus used in this project is a unique triaxial cell that was designed for the measurements of undrained dynamic elastic moduli of rock specimens at seismic frequencies (0.1-155 Hz) as well as ultrasonic P- and S-wave velocities (500 kHz) under various stress conditions, with independent control of axial stress, radial stress and pore pressure. It should be noted that there are only a few other laboratories in the world that can perform dynamic-stiffness measurements at seismic frequencies (e.g. Batzle et al., 2006; Tisato and Madonna, 2012; Mikhaltsevitch et al., 2014; Pimienta et al., 2015; Spencer and Shine, 2016; Szewczyk et al., 2016). A sketch of the low-frequency setup is shown in Figure 2. Ultrasonic measurements are done by the standard pulse transmission technique. The strain amplitudes of ultrasonic measurements are small, in the order of 10^{-7} - 10^{-6} strains (Tutuncu et al., 1998; Fjær et al., 2008). For the measurements of the dynamic elastic moduli (Young's modulus and Poisson's ratio in two orthogonal directions), the sample is excited by a displacement actuator at a given frequency within the seismic band. The resulting force modulation is measured by a piezoelectric force sensor, and the strain modulations are measured by strain gages attached to the sample surface. Strain-modulation amplitudes are kept below 10^{-6} in order to stay in the elastic regime (for higher strain-amplitudes, the dynamic stiffness is impacted by non-elastic effects, see (Batzle et al., 2006; Lozovyi et al., 2017). A detailed description of the apparatus is given in (Szewczyk et al., 2016).

For anisotropic media, Young's moduli and Poisson's ratios are direction dependent. For transverse-isotropic (TI) media, there are five independent stiffness parameters (compared to two independent stiffness parameters for isotropic media) (Nye, 1984), and with the present experimental setup, dynamic stiffness measurements have to be carried out with three differently oriented samples in order to determine all 5 independent stiffness parameters as well as P- and S-

wave moduli from which P- and S-wave velocities can be calculated. Errors occur if the three differently oriented samples do not have identical mechanical properties, which make an accurate determination of seismic P- and S-wave moduli and velocities difficult. In the course of this project, it was demonstrated (Lozovyi & Bauer, manuscript in preparation) that the seismic P-wave modulus for P-wave propagation perpendicular to bedding can directly be measured (so far only at frequencies ≤ 1 Hz) by modulating both the axial stress and the confining stress (the latter by a small piston driven by a stepper motor) in such a way (amplitudes and phases need to be synchronized) that a radial-strain modulation is suppressed (uniaxial-strain conditions). First results with Opalinus Clay are presented in this paper.

2.3 Test protocol

All tests were carried out at room temperature. The samples were stabilized at two different stress states (see Figure 3A):

- Lower stress state ("L"): Confining stress, p_{conf} = 7 MPa; axial stress, σ_{ax} = 7 MPa; pore pressure, p_f = 3 MPa (net stress, $p_{conf}' = p_{conf} - p_f$ = 4 MPa).
- Higher stress state ("H"): p_{conf} = 13 MPa; σ_{ax} = 13 MPa; p_f = 3 MPa (net stress, p_{conf}' = 10 MPa).

At both stress states, undrained loading/unloading cycles (5 MPa/h loading rate) were performed. For the first set of tests (sandy facies #1), a stress amplitude of 4 MPa was applied. However, this relatively large stress amplitude resulted in higher than expected irreversible sample deformations, so the stress amplitude was reduced to 1 MPa for the remaining tests. Compressional and shear-wave ultrasonic signals were recorded continuously throughout the experiment. The experiments were carried out for three different sample-axis orientations: 0°, 45°, and 90° with

respect to the bedding plane (see Figure 4 for the angle convention used here), to obtain the static and dynamic TI stiffness-matrix components.

To check for repeatability, each test was repeated with another core plug from the same facies, following a reduced test protocol (see Figure 3B). In the repeat tests, the samples were only brought to the lower stress state (p_{conf} = 7 MPa; σ_{ax} = 7 MPa; p_f = 3 MPa).

Since the low-frequency measurements require a finite deviatoric stress ($\sigma_{ax} > p_{conf}$), for both stress states, the axial stress was increased by 1 MPa after the loading/unloading cycles are completed. It is evident that this additional axial stress – as compared to the isotropic stress state – has a very little effect on the dynamic stiffness and accounted in systematic error stated in the results.

The following quantities were recorded during all tests: axial and radial stresses, pore pressure, axial and radial sample deformations (axial and radial strains) measured by strain gages attached to the sample, axial strain measured by LVDTs, compressional and shear-wave ultrasonic (phase) velocities, V_P and V_S, in axial direction, using the standard pulse-transmission technique.

It should be noted that the shear-wave (S-wave) signals were superposed by converted P-wave signals, which made it in some cases impossible to identify the S-wave arrival and to determine the S-wave velocity.

During the low-frequency measurements, an axial force modulation is generated by a piezoelectric actuator (integrated in sample stack), and the following quantities are recorded as a function of frequency (1 Hz – 150 Hz):

- Axial strain modulation (amplitude and phase) measured by strain gages attached to the sample;

- Radial strain modulation (amplitude and phase) measured in two orthogonal directions by strain gages attached to the sample;
- Axial-force modulation measured by a piezoelectric force sensor (integrated in the sample stack).

2.4 Data analysis

2.4.1 Skempton parameters

Pore-pressure changes, Δp_f, during undrained loading can be described by the Skempton A and B parameters defined by (Skempton, 1954):

$$\Delta p_f = B\left(\Delta p_{conf} + A\left(\Delta\sigma_{ax} - \Delta p_{conf}\right)\right) \quad (1)$$

For isostatic loading ($\Delta\sigma_{ax} = \Delta p_{conf}$), one gets:

$$B = \frac{\Delta p_f}{\Delta p_{conf}} \; . \quad (2)$$

For soft rocks, B is close to one, which means that any additional load is «carried» by the pore fluid. A low B value is often an indication for a partially saturated rock.

For triaxial loading ($\Delta p_{conf} = 0$), the change in pore pressure is given by $\Delta p_f = B \cdot A \cdot \Delta\sigma_{ax}$, which can be used to calculate A:

$$A = \frac{1}{B} \cdot \frac{\Delta p_f}{\Delta\sigma_{ax}} \quad (3)$$

2.4.2 Static stiffness

Isotropic media are characterized by two independent stiffness parameters, e.g. Young's modulus and Poisson's ratio. For anisotropic media, the elastic properties are characterized by more than two independent parameters, and static compression measurements with several samples are needed for a full stiffness characterization. In case of TI symmetry that is assumed here for Opalinus Clay, with the symmetry axis perpendicular to bedding, static compression measurements have to be performed for three different sample orientations (using a triaxial cell). In the present case, the following stiffness parameters are measured with 0°, 45°, and 90° oriented samples for undrained loading (drained stiffness is not measured in this project): Bulk modulus, K, Young's modulus, E_V, and Poisson's ratio, ν_{VH}, measured with the 90° sample; E_H measured with the 0° sample; E_{45} measured with the 0° sample. From those 5 parameters, the 5 independent stiffness-matrix components, C_{11}, C_{33}, C_{13}, C_{44}, C_{66}, can be calculated by using the following relations for media with TI symmetry (Nye, 1984; Bower, 2010):

$$C_{33} = E_V\,(1 - \nu_{HH}^2)\,\Lambda$$

$$C_{11} = E_H\,(1 - \nu_{HV}\nu_{VH})\,\Lambda$$

$$C_{13} = E_H\,\nu_{VH}\,(1 + \nu_{HH})\,\Lambda \qquad (4)$$

$$C_{44} = \left[\frac{4}{E_{45}} - \frac{1}{E_V} - \frac{1}{E_H} + \frac{C_{13}}{(C_{11} - C_{66})C_{33} - C_{13}^2}\right]^{-1}$$

$$C_{66} = \frac{E_H}{2(1 + \nu_{HH})}$$

with

$$\nu_{HV} = \nu_{VH}\frac{E_H}{E_V}$$

$$\nu_{HH} = 1 - 2\nu_{HV} - \frac{E_H}{2}\left(\frac{1}{K} - \frac{1}{E_V}\right)$$

$$\Lambda = [1 - \nu_{HH}^2 - 2\nu_{HV}\nu_{VH} - 2\upsilon_{HH}\upsilon_{HV}\upsilon_{VH}]^{-1}$$

2.4.3 Dynamic stiffness and velocities at seismic frequencies

In a low-frequency measurement, dynamic Young modulus and Poisson ratio are measured as a function of frequency in the frequency range from 1 Hz to 150 Hz (Szewczyk et al., 2016). For isotropic media, this data can readily be converted to P-wave modulus and shear modulus, from which, together with the rock density, P- and S-wave velocities can be calculated. For transverse isotropic (TI) media, there are 5 independent stiffness parameters, and low-frequency measurements with three differently oriented samples are needed for a full characterization of the elastic properties. In this work, the following six stiffness parameters are measured: Young's moduli E_V (measured with the 90° sample), E_H (measured with the 0° sample) and E_{45} (measured with the 45° sample), and Poisson's ratios, ν_{VH} (measured with the 90° sample), and ν_{HV} and ν_{HH} (measured with the 0° sample). For a rock with TI symmetry, only five of these six parameters are independent. It can be shown that (Holt, 2016)

$$\left(\frac{E_V}{E_H}\right)/\left(\frac{\nu_{VH}}{\nu_{HV}}\right) = 1 \qquad (5)$$

A deviation of the term on the left side of Eq. (5) from 1 is an indication for rock heterogeneity (E_V and ν_{VH}, and E_H and ν_{HH} are measured with two different samples, respectively), a deviation from TI symmetry and/or experimental uncertainty. However, for small deviations, the assumption of TI symmetry may still be acceptable, and the commonly used stiffness matrix, C_{ij},

with the 5 independent parameters C_{11}, C_{33}, C_{44}, C_{66}, and C_{13} can be obtained from the measured 6 parameters by a least-square fit routine (here, it is assumed that the relative error of the Poisson ratios is twice as large as that of the Young moduli since the error is mainly due to the error of the strain-gage readings, and Poisson's ratio is the ratio between radial and axial strain, while Young's modulus depends only on the axial strain). The error of the stiffness-matrix elements, C_{ij}, is relatively high: A recent systematic error analysis based on measurements with an aluminium sample, including both systematic and random errors (Lozovyi & Bauer, manuscript in preparation), shows that the obtained C_{ij} values are smaller than the real values with an error between 0% and 20% (the relative error of the obtained velocities is only half as large since velocities are given by the square root of the respective moduli). For heterogeneous, anisotropic materials, the errors in the C_{ij} values may even exceed 20% but it is difficult to quantify the error. The error of the P-wave modulus, C_{33}, can be strongly reduced by direct P-wave-modulus measurements as developed during the course of this project. The estimated error of the P-wave modulus obtained by direct P-wave-modulus measurements is 6% (3% for the P-wave velocity). It is also less affected by heterogeneity since the P-wave modulus is measured with a single sample.

The relations between the measured parameters (E_V, E_H, E_{45}, ν_{VH}, ν_{HV} and ν_{HH}) and the stiffness-matrix parameters (C_{11}, C_{33}, C_{44}, C_{66}, and C_{13}) are as follows:

$$
\begin{aligned}
E_V &= C_{33} - \frac{C_{13}^2}{C_{11}-C_{66}} \\
E_H &= \frac{4C_{66}[(C_{11}-C_{66})C_{33}-C_{13}^2]}{C_{11}C_{33}-C_{13}^2} \\
E_{45} &= 4\left[\frac{1}{E_V}+\frac{1}{E_H}+\frac{1}{C_{44}}-\frac{C_{13}}{(C_{11}-C_{66})C_{33}-C_{13}^2}\right]^{-1} \\
\nu_{VH} &= \frac{C_{13}}{2(C_{11}-C_{66})} \\
\nu_{HV} &= \frac{2\,C_{66}\,C_{13}}{C_{11}C_{33}-C_{13}^2} \\
\nu_{HH} &= \frac{(C_{11}-2C_{66})C_{33}-C_{13}^2}{C_{11}C_{33}-C_{13}^2}
\end{aligned}
\tag{6}
$$

P- and S-wave velocities perpendicular to bedding, V_{PV} and V_{SV}, and parallel to bedding, V_{PH} and V_{SH} (here, V_{SH} is the velocity of the S-wave with polarization within in the bedding plane), are given by:

$$
\begin{aligned}
\mathrm{V_{PV}} &= \sqrt{C_{33}/\rho} \\
\mathrm{V_{PH}} &= \sqrt{C_{11}/\rho} \\
\mathrm{V_{SV}} &= \sqrt{C_{44}/\rho} \\
\mathrm{V_{SH}} &= \sqrt{C_{66}/\rho}
\end{aligned}
\tag{7}
$$

Here, ρ is the rock density (taken as average of the densities of the three samples the low-frequency measurements have been carried out with). In addition to the seismic velocities, the Thomsen anisotropy parameters, ε, γ, and δ, can be calculated from the stiffness-matrix parameters C_{11}, C_{33}, C_{44}, C_{66}, and C_{13}, using well-known relations (Thomsen, 1986):

$$
\begin{aligned}
\varepsilon &= \frac{C_{11}-C_{33}}{2\,C_{33}} \\
\gamma &= \frac{C_{66}-C_{44}}{2\,C_{44}} \\
\delta &= \frac{(C_{13}+C_{44})^2-(C_{33}-C_{44})^2}{2\,C_{33}(C_{33}-C_{44})}
\end{aligned}
\tag{8}
$$

2.4.4 Ultrasonic velocities

Ultrasonic phase velocities are measured by the conventional pulse-transmission technique. Home-built compressional (P) and shear-wave (S) piezoelectric transducers with a resonance frequency of 500 kHz are integrated in the endcaps of the sample. A pulse (one period of a sinewave with a frequency of 500 kHz) is transmitted by a transducer on one side of the sample and received after a certain travel time by the respective transducer on the other side of the sample. From the travel time (corrected for the time of transmission through the Titanium plates between sample and transducers) and the actual length of the sample, the velocities are calculated. Calibration measurements are carried out with an aluminium sample with known ultrasonic velocities.

From the measured P- and S-wave velocities for 0°, 45°, and 90° oriented samples, the dynamic stiffness-matrix elements can be calculated by applying Eq. (7), and the following relation for C_{13} for TI symmetry (Mavko et al., 2009):

$$C_{13} = C_{44} + \sqrt{4\rho^2 V_{P45}^4 - 2\rho V_{P45}(C_{11} + C_{33} + 2C_{44}) + (C_{11} + C_{44})(C_{33} + C_{44})}\ , \qquad (9)$$

with V_{P45} the P-wave phase velocity along the axis of a 45°-oriented sample.

The Thomsen anisotropy parameters are obtained by applying Eq. 8.

3 Experimental results

In total, 4 sets of experiments have been carried out, each set consisting of 3 tests with differently oriented samples (0°, 45°, and 90°) from equal or similar depth. Sets 2 and 4 are repeat experiments with a reduced test protocol (lower stress state only).

A typical timeline of measured stresses and strains is shown in Figure 5.

Axial strains are measured both with three LVDTs, and strain gages attached to the sample at mid height. Radial strains are only measured by strain gages. For sample-length corrections used for the analysis of the ultrasonic data, the LVDT data is used. For the determination of static and dynamic stiffness, the strain-gage data is used. There are rather large deviations between LVDT and strain-gage signals during initial loading and consolidation but during the undrained loading/unloading cycles, the LVDT and strain-gage signals are consistent. Deviations between LVDT and strain-gage signals may be due to sample heterogeneity: Strain gages measure the strain in the middle of the sample over a distance of about 3 mm, while the LVDTs measure the total-length change. The large discrepancies in the beginning of the test, during loading and consolidation, are not fully understood yet. They may be related to non-uniform drainage and thus a non-uniform strain distribution (the metal mesh that is wrapped around the sample for enhanced drainage has cut-outs in the areas where the strain gages are placed). We can also not exclude some initial relaxation of the strain gages that are hold in place by friction forces (the gages are not glued to the sample surface). Since only data from the loading/unloading cycles is used for the data analysis, these initial discrepancies between LVDT and strain gage signals are of no relevance.

3.1 Consolidation effects

Consolidation after reaching a given stress state took between 1 and 2 days. In order to proceed with static or dynamic measurements the issue of rock stiffness dependence on a consolidation (creep) rates had to be studied. Both for the sandy facies (with sample 2-90), and for the shaly facies (with sample 4-90), low frequency measurements were carried out at different creep rates (axial-strain rates) during consolidation period. For the sandy facies, no significant stiffness changes (< 1%) were measured for axial-strain rates smaller than 0.4 μstrain/h (see Table 2 and

Figure 6). Core plugs from the shaly facies exhibited stronger creep. However, the rock stiffness does not change any longer (< 1%) for axial-strain rates as high as 50 μstrain/h (see Table 3 and Figure 6).

3.2 Skempton parameters

Skempton A and Skempton B values obtained during single undrained unloading sequences at the two different stress states are summarized in Table 4.

The Skempton B parameter is consistently around 0.9 both for the sandy and the shaly facies at the lower stress state and around 0.8 for the higher stress state, with the exception of sample 1-90 where the Skempton B parameter slightly increases to 0.92 at the higher stress state. The Skempton A parameter is dependent on sample orientation. The orientation dependence is largest for the shaly facies (the shaly facies exhibits also larger stiffness anisotropy as will be discussed below) where it varies between about 0.13 for 0° orientation and up to 0.6 for 90° orientation. For the sandy facies, the Skempton A parameter varies between about 0.15 for 0° orientation and up to 0.45 for 90° orientation. Anisotropy effects of the Skempton A parameter have previously been observed for other shales as well (Holt et al., 2017).

3.3 Static stiffness – non-elastic effects

Compared to other shales, Opalinus Clay exhibits large non-elastic effects (hysteresis in stress-strain curves) during undrained loading and unloading. Figure 7 shows the stress-strain data recorded with sample #2-90 during three subsequent undrained triaxial loading/unloading cycles with different stress amplitudes. In the first cycle, the axial stress was increased by 1 MPa, in the second cycle by 2 MPa, and in the third cycle by 4 MPa (loading rate 5 MPa/h). Both for loading and unloading, the incremental compliance (inverse of the incremental stiffness), $d\varepsilon_{ax}/d\sigma_{ax}$, is low in

the beginning and increases gradually as the change in axial stress, $\Delta\sigma_{ax}$, increases. At the end of the loading (unloading) sequence, at constant stress, some creep is observed that increases with stress amplitude, and is largely reversible. The creep effects will not be investigated in this paper.

In agreement with previous studies with sandstones and shales (Fjær et al., 2013), $d\varepsilon_{ax}/d\sigma_{ax}$, is a linear function of $\Delta\sigma_{ax}$ (see Figure 8). It is interesting to note that the compliance at $\Delta\sigma_{ax} = 0$ is nearly the same for all three cycles, while the average stiffness, $\Delta\sigma_{ax}/\Delta\varepsilon_{ax}$, strongly diminishes with increasing stress amplitude. This is illustrated in Figure 9, where the average undrained Young's modulus, $E_u = \Delta\sigma_{ax}/\Delta\varepsilon_{ax}$, is plotted as a function of $\Delta\sigma_{ax}$, together with the zero-stress extrapolated value, $(d\varepsilon_{ax}/d\sigma_{ax})_0$. By assuming a linear relationships between $d\varepsilon/d\sigma_{ax}$ and $\Delta\sigma_{ax}$ with a slope of C, the average stiffness can be expressed by a quadratic function in $\Delta\sigma_{ax}$ (Lozovyi et al., 2017):

$$\frac{\Delta\varepsilon}{\Delta\sigma_{ax}} = \left(\frac{d\varepsilon}{d\sigma_{ax}}\right)_0 + \frac{C}{2}\cdot\Delta\sigma_{ax} \tag{11}$$

For the particular case shown in Figure 9, $(d\varepsilon_{ax}/d\sigma_{ax})_0 \approx 0.20$ GPa^{-1}, and $C \approx 9\cdot10^{-5}$ MPa^{-2}.

Lozovyi et al. (2018) have shown that the Eq. 11 can be used to model the non-elastic effects in both axial and radial strains, ε_{ax} and ε_{rad}, as function of axial stress change, $\Delta\sigma_{ax}$. This allows for finding zero-stress extrapolated Young's moduli and Poisson's ratios.

For each sample and for both reference stress states (lower stress state: p_{conf} = 7 MPa, p_f = 3 MPa; higher stress state: p_{conf} = 13 MPa, p_f = 3 MPa), the average undrained bulk modulus and Young's modulus are determined from the unloading sequences of the undrained isostatic and undrained triaxial loading/unloading cycles. For each set of tests with differently oriented samples, following the procedure described in Chap. 2.4.2, the 5 independent stiffness-matrix parameters C_{11}, C_{33}, C_{44}, C_{66}, and C_{13}, are calculates (see Table 5 and Table 6).

For the static measurements presented in Table 5 and Table 6, the magnitude of error could be estimated from two independent strain measurements: LVDTs and strain gages. Using these strains to calculate static moduli and Poisson's ratio resulted in discrepancies of about 5-10%, in some cases up to 20%. However, since strain gages measure local deformation and LVDT average it over the sample's length, the difference between LVDT and strain gage data is partly caused by heterogeneities of the sample. The static data presented in the paper is calculated using only the strains recorded with strains gages. The same gages are used for dynamic measurements at seismic frequencies.

For homogeneous material, the bulk modulus should be the same for all core plugs from the same facies. However, within each set of samples, the bulk modulus varies by up to more than ± 10% for the shaly facies and nearly ± 30% for the sandy facies, which indicates rather large heterogeneity. As a consequence, the calculated stiffness-matrix parameters, C_{ij}, are also affected by heterogeneity, with expected errors of the order of ± 10% for the shaly facies and even more for the sandy facies.

For set #1 (sandy facies), the Young modulus of the 45° sample, E_{45}, is almost as large as of 0° sample, which would mean that C_{44} would be greater than C_{66} (negative Thomsen γ parameter). This does not seem to be physical and can most likely be attributed to rock anisotropy. The derived stiffness-matrix parameters, C_{44} (the only parameter that depends on E_{45}), obtained from set #1 is therefore considered unreliable. The results obtained with the second sandy-facies set #2 are more plausible. Here, C_{44} is smaller than C_{66}.

Altogether, large stiffness anisotropies are measured. Very large anisotropies are observed for the shear stiffness as can be seen by comparing C_{44} and C_{66}.

As discussed above, the average static moduli listed in Table 5 and Table 6 account for both elastic and non-elastic deformations, and depend on the stress-change amplitude. The purely elastic moduli can be obtained by extrapolation of the incremental compliances $d\varepsilon_{ax}/d\sigma_{ax}$ and $d\varepsilon_{rad}/d_{\sigma ax}$ to zero stress change ($\Delta\sigma_{ax} = 0$) as demonstrated on Figure 8 with red dots for sample 2-90.

Zero-stress extrapolated compliances, $(d\varepsilon_{rad}/d\sigma_{ax})_0$ and $(d\varepsilon_{ax}/d\sigma_{ax})_0$, will give a zero-stress extrapolated Young's modulus, E_0, and Poisson's ratio, ν_0:

$$E_0 = \frac{1}{(d\varepsilon_{ax}/d\sigma_{ax})0} \tag{12}$$

$$\nu_0 = -\frac{(d\varepsilon_{rad}/d\sigma_{ax})0}{(d\varepsilon_{ax}/d\sigma_{ax})0} \tag{13}$$

The resulting zero-stress extrapolated moduli (and Poisson's ratios) are listed in Table 7 and Table 8. Please note that very high Poisson's ratios (close to 0.5, see Table 5) measured for finite stress amplitude with samples 1-90 and 2-90 are caused by strong non-linear effects in stress-strain relations. The zero-stress extrapolated values of Poisson's ratios (shown in Table 7) are much lower and represent purely elastic response (unaffected by non-linear effects).

As expected, the zero-stress extrapolated elastic stiffness parameters are systematically larger than the average stiffnesses listed in Table 5 and Table 6.

3.4 Dynamic stiffness and velocities at seismic frequencies

In Figure 10 – Figure 13, the measured dynamic undrained Young's moduli and Poisson's ratios are plotted as a function of frequency for the for different sets of experiments and for both stress states (lower stress state "(L)": p_{conf} = 7 MPa, p_f = 3 MPa; higher stress state "(H)": p_{conf} = 13 MPa, p_f = 3 MPa). Included in the plots is also the ratio $(E_V/E_H)/(\nu_{HV}/\nu_{VH})$, which for TI symmetry

should be equal to one. For set #1 (sandy facies), the ratio is as low as 0.65, which is far from the theoretical value of one. For set #2 (sandy facies), the ratio is around 0.9, which is in reasonable agreement with TI symmetry. For sets #3 and #4, the ratios were larger than 1 and as high as 1.2. Interestingly, for set #3, the ratio was close to the theoretical value of 1 at the higher stress state, which could indicate that the TI symmetry is restored at higher stresses. In summary, except for set #1, the experimental data is reasonably consistent with TI symmetry; deviations of the measured ratio from the theoretical value of 1 is attributed to cm-scale stiffness heterogeneity.

For the first set of samples (sandy facies, samples 1-0, 1-45, 1-90), the Young modulus of the 45°-oriented sample is higher than that of the 0°-oriented sample, which is not consistent with TI symmetry. It is likely that this inconsistency is due to rock heterogeneity. For sets #2, #3, and #4, special care was taken to identify homogeneous zones in the core and get sets of plugs with as small a distance perpendicular to bedding as possible (assuming that the rock is more homogeneous parallel to bedding). Indeed, for the sets #2, #3, and #4, heterogeneity effects were smaller, but the experimental data was still not fully consistent with TI symmetry. It is interesting to note that for the shaly facies, the Young moduli of the 45° and 90° samples are consistently nearly the same. This is consistent with TI symmetry and indicates large anisotropy (high Thomsen γ, see below).

Both samples from the sandy facies and the shaly facies exhibit relatively strong Young-modulus dispersion (i.e. a frequency dependence of the dynamic Young modulus) but little or no dispersion of the Poisson ratios within tested seismic frequency band.

A comprehensive error analysis of the low-frequency measurement has shown that the uncertainties are mostly dominated by systematic errors (Lozovyi & Bauer, manuscript in preparation). The systematic error of Young's modulus is estimated in a range of -4% - 0% independently of measured direction (E_V, E_H or E_{45}). For Poisson's ratio, the systematic error is

dependent on the direction of the measurement. The highest error is up to -6.5% for ν_{HH} and the lowest error is up to -4% for ν_{HV}. Random errors are 0.7% for Young's modulus and 2.3% for Poisson's ratio.

By applying the procedure described in Chap. 2.4.3, the stiffness-matrix elements C_{11}, C_{33}, C_{44}, C_{66}, and C_{13}, and the seismic P- and S-wave velocities perpendicular to bedding, V_{PZ} and V_{SZ}, and Thomsen anisotropy parameters, ε, γ, and δ, are determined from the measured Young's moduli and Poisson's ratios. The results are shown in Figure **14** and Figure **15**. Note the large shear-stiffness anisotropy (the difference between C_{44} and C_{66}, resulting in a very high Thomsen γ), which is consistent with the high static shear-stiffness anisotropy (see Tables 5 – 8). Altogether, the dynamic stiffness parameters at low seismic frequencies (1 Hz) are close to the zero-stress extrapolated static stiffness parameters (see Table 7 and Table 8).

3.4 Ultrasonic velocities

P-wave phase velocities parallel to the sample axis were measured for all samples and are listed for the lower stress state and the higher stress state in Table 9.

S-wave velocities could not be always determined, especially for the sandy facies. Because of a relatively strong converted P-wave signal that was superposed on the S-wave signal, it cannot be excluded that wrong S-wave arrivals were picked from the waveforms, resulting in large errors of the S-wave velocities. Typical P- and S-waveforms are shown in Figure 16. In the absence of S-wave velocities, the Thomsen anisotropy parameters γ and δ could not be determined for the sets 1 and 2 of the sandy facies and at the higher stress state for the set 3 of the shaly facies.

Available Thomsen anisotropy parameters and dynamic stiffness parameters at ultrasonic frequency derived from velocity measurements under three orientations are also listed in Table 9.

4 Discussion

Shaly facies versus sandy facies

The sandy facies is more heterogeneous than the shaly facies, which made it difficult to get a set of differently oriented samples with the same mechanical properties. Especially for set #1 but to some extent also for set #2, quantities that were calculated based on measurements with differently oriented samples (stiffness-matrix parameters and velocities from static and dynamic stiffness measurements) may not be reliable. Because of the large heterogeneity of the sandy facies it is not clear how representative the present results are and how big the variability of the rock stiffness is within the sandy facies. For the shaly facies, on the other hand, the results obtained with two sets of samples are consistent, which indicates that the results are representative for the shaly facies in the area the core was taken.

Nevertheless, the experimental data consistently shows that both the static stiffness, the dynamic stiffness at seismic frequencies, and the ultrasonic velocities (P-wave velocities) are higher for the sandy facies than for the shaly facies. The stiffness anisotropy and velocity anisotropy are significantly lower for the sandy facies than for the shaly facies. Both sandy facies and shaly facies exhibit significant seismic dispersion, but due to experimental uncertainties and heterogeneity effects it is difficult to say if the magnitude of dispersion is different for the two facies. There are also strong non-elastic effects observed for both facies, which means that the average stiffness is a function of stress amplitude (both for loading and unloading).

Stress dependence of rock mechanical properties

Overall, hydrostatic-stress increase (from p_{conf} = 7 MPa to p_{conf} = 13 MPa, or, respectively, from p_{conf}' = 4 MPa to p_{conf}' = 10 MPa) resulted in an increased rock stiffness and increased seismic

and ultrasonic velocities. However, for several samples, the static bulk modulus was smaller at the higher stress state.

The undrained stress cycles performed at the lower stress have in some cases (e.g. for set #1 and for sample 3-90 where undrained stress cycles with higher stress amplitude were performed) resulted in some irreversible rock deformations. It cannot be excluded that those deformations resulted in stiffness alterations so that the moduli measured at the higher stress state after the alterations have occurred are not comparable with the moduli measured at the lower stress state before the alterations were induced. In future experiments, stress cycles should be performed with as small an amplitude as possible (1 MPa or lower) to minimize plastic rock deformations and rock-stiffness alterations.

Anisotropy

Both the sandy facies and the shaly facies exhibit large anisotropy of both static and dynamic stiffness (see Table 5 - Table 8, Figure **14** - Figure **15**). It is interesting to note that the present static-stiffness data indicates very high Thomsen γ values (shear-modulus anisotropy, see Eq. 8) of > 0.5 (large experimental uncertainties due to rock heterogeneity). The γ values determined from the low-frequency data are around 0.3 for the sandy facies (set #2, lower stress state), and between $\approx$ 0.7 (set #4, lower stress state) and around 0.8 (set #3, higher stress state) for the shaly facies. Those high γ values are consistent, at least for the shaly facies. The ultrasonic velocity measurements are in reasonable agreement (given the uncertainties) with seismic measurements, resulting in γ values of $\approx$ 0.72 and 0.85 for sets #4 and #3 respectively at lower stress state. Due to strong adsorption and P-wave conversion, it was only possible to measure S-wave velocities with samples from shaly facies. The high shear-modulus anisotropy can probably be attributed to weakly bound bedding layers.

Seismic dispersion

The low-frequency measurements revealed relatively large dispersion of Young's modulus (increase by more than 10% between 1 Hz and 100 Hz) and nearly no dispersion of Poisson's ratio within the seismic band for both the sandy and the shaly facies. Large dispersion is also observed in the S-wave velocities, V_{SV}, that were calculated from the Young's modulus and Poisson's ratio data measured with three differently oriented samples (see Figure 17 - Figure 20). Due to noise in the Poisson's-ratio data and a high sensitivity of P-wave velocities to the Poisson ratio, the calculated P-wave velocities, V_{PV}, are in some cases rather noisy, and the dispersion of the P-wave velocity is not as clearly visible as for V_{SV}. For the sandy facies (set #2), the seismic V_{PV} values are by about 400 m/s smaller than the ultrasonic V_{PV}, which corresponds to a velocity dispersion of about 15% between seismic and ultrasonic frequencies (see Figure **18**). Low-frequency measurements with the sandy-facies core plugs from set #1 indicate an even stronger dispersion (more than 40% at the lower stress state and about 26% at the higher stress state; seeFigure **17**). It is, however, questionable if the calculated seismic velocities are reliable since the three plugs from set #1 were found to have different mechanical and mineralogical properties. For the shaly facies, the seismic V_{PV} values are by about 300-400 m/s smaller than the ultrasonic V_{PV}, which corresponds to a velocity dispersion of 12 - 18% between seismic and ultrasonic frequencies (see Figure **19** and Figure 20).

Due to rock heterogeneity and the fact that seismic velocities are calculated based on measurements with three different samples, there is potentially a sizable error in the seismic-velocity data. This error is difficult to quantify as it depends on the degree of heterogeneity. In order to reduce the error for P-wave velocities, a new method was developed during the course of this project, allowing for the direct measurements of the dynamic P-wave modulus at low frequencies

(see Chap. 2.2). First results obtained for the shaly facies (lower stress state, frequency of 1 Hz) indicate that V_{PV} is about 5-6% higher for set #3 and about 12% higher for set #4 than the respective values obtained from Young's-modulus and Poisson's-ratio measurements with three differently oriented samples (see filled symbols in Figure 19 and Figure 20). It is not yet certain how reliable the direct P-wave modulus measurements are, however recent calibration measurements with an aluminium sample indicated an error of about -3% for the P-wave velocity. This is a significant improvement compared to the conventional method with 3 differently oriented plugs, there, the error in P-wave velocity could be up to -10% and more (depending on the degree of core heterogeneity).

Static versus dynamic stiffness

The laboratory measurements with Opalinus Clay, both for the sandy facies and the shaly facies, have revealed a large impact of non-elastic effects on the static stiffness. It turns out that the incremental compliances for undrained loading/unloading, $d\varepsilon_{ax}/d\sigma_{ax}$, and $d\varepsilon_{rad}/d\sigma_{ax}$, increase linearly with stress both during unloading and loading according to Eq. 11. The compliances extrapolated to zero change in stress ($\Delta\sigma_{ax} = 0$), $(d\varepsilon_{ax}/d\sigma_{ax})_0$ and $(d\varepsilon_{rad}/d\sigma_{ax})_0$ are interpreted to represent the purely elastic response that is also measured with small-strain ($< 10^{-6}$) dynamic measurements at low seismic frequencies (see Figure **21** on the example of Young's modulus). Sandy and shaly facies exhibit similar non-elastic effects: For triaxial unloading, the non-elasticity constant, C, was found to be about $9 \cdot 10^{-5}$ MPa^{-2} for the sandy facies and $7 \cdot 10^{-5}$ MPa^{-2} for the shaly facies. The difference is within the experimental uncertainty (for sandy facies, the C value varied from $7 \cdot 10^{-5}$ MPa^{-2} to $11 \cdot 10^{-5}$ MPa^{-2}).

With increasing frequency, the dynamic stiffness increases (Figure **21**). The dispersion mechanisms are not fully understood yet but it may be related to local flow of bound water at grain contacts (Szewczyk et al., 2018).

Static and dynamic stiffnesses are also influenced by visco-elastic/plastic effects (consolidation or creep effects). Those consolidation or creep effects result in a slightly lower stiffness (by about 5-10%). It can be shown that the loading rates used in the present experiments (5 MPa/h) correspond to the average absolute value of the loading rate during dynamic measurements at a frequency of about 0.5 Hz (for strain-modulation amplitudes of about 10^{-6} as used in the present work). Stiffness obtained from the stress-strain slopes correspond therefore to quasi-static stiffness at around 0.5 Hz. By including strain relaxation during the consolidation phase, the static stiffness is obtained (indicated by arrows in Figure **21**). As seen in Figure **21**, consolidation or creep effects have only a minor impact on the stiffness of Opalinus Clay.

5 Conclusions

In this paper, the static and dynamic stiffness of two facies of Opalinus Clay have been measured. The experiments were carried out in SINTEF's low frequency apparatus that allows for combined measurements of static compression, dynamic stiffness at seismic frequencies, and ultrasonic velocities under different stress and pore pressure conditions. In total, 4 sets of experiments have been carried out, two sets with core plugs from the sandy facies, and two with core plugs from the shaly facies. Each set of experiments consisted of three tests with differently oriented core plugs (0°, 45°, and 90° with respect to bedding), which allowed for a complete characterization of both static and dynamic stiffness anisotropy (assuming TI symmetry). The results gave invaluable insights in the relation been the static undrained stiffness accounting for rock deformation under stress, and the dynamic stiffness and acoustic velocities at seismic and ultrasonic frequencies. The obtained results clearly show that the difference between static and dynamic stiffness is due to both dispersion (frequency dependence) and non-elastic effects (stress dependence).

Both tested facies of Opalinus Clay show considerable velocity dispersion. For the P-wave velocity perpendicular to bedding, the dispersion amounts to ~200m/s for the shaly facies between lower seismic (0.5 Hz) to ultrasonic (500 kHz) frequencies. For the sandy facies, the experimental data indicates even higher velocity dispersion. However, due to a high degree of heterogeneity of the sandy facies and the fact that the seismic velocity data is derived from sets of differently oriented samples, resulting in high velocity errors (up to more than 10%). The observed difference between vertical P-wave modulus (C_{33}) measured at seismic and ultrasonic frequency is around 20% for the shaly facies. For the vertical Young modulus, E_V, the difference is even more pronounced: E_V measured at 1 Hz is by a factor 2 lower than E_V estimated from ultrasonic measurement (see Figure **21**, right). Nearly the same difference is observed for the horizontal Young modulus, E_H. This high dispersion effect on Young's modulus may be explained by a strong decrease of Poisson's ratio (both ν_{VH} and ν_{HV}) from seismic to ultrasonic frequencies. The mechanisms of these large dispersion effects are not understood yet. It was recently suggested that in shales it might be related to a local flow of bound water at grain contacts (Szewczyk et al., 2018).

The static undrained stiffness of both the sandy and the shaly facies, even for small stress changes, is strongly influenced by non-elastic effects, resulting in significant softening during both loading and unloading with increasing stress amplitude. The static undrained Young modulus, E_V, measured for a stress amplitude of 4 MPa is by almost a factor of 2 lower than that measured for a 1 MPa stress cycle (see Figure **21**, left). The zero-stress extrapolated static undrained stiffness agrees well with the dynamic stiffness at small seismic frequencies (strain amplitudes $< 10^{-6}$ for the dynamic measurements). The non-elastic effects can be described by a linear relationship between compliance and stress-change amplitude. In this way, it is possible to derive the static undrained stiffness for any given change in stress from seismic measurements and vice versa. The linear

dependence of the compliance with stress amplitude was found empirically by Fjær et al. (2011) and verified for different sedimentary rocks (Fjær et al., 2012, 2013; Holt et al., 2012). Lozovyi et al. (2017) have shown that the empirical model is applicable down to the micro-strain amplitudes.

Altogether, including non-elastic effects and dispersion effects, we observe differences between dynamic Young's moduli at ultrasonic frequencies (converted from ultrasonic velocities) and static undrained Young's modulus (for a 4 MPa stress amplitude) of at least a factor of 3.5 for both the sandy and the shaly facies of Opalinus Clay. Both stress amplitude and frequency play significant roles here.

The shaly facies exhibits a significantly higher anisotropy than the sandy facies of both static and dynamic stiffness. Especially the shear stiffness is highly anisotropic for the shaly facies (large difference between C_{44} and C_{66}; high Thomsen γ values), which may be the result of weakly bounded bedding planes. This assumption is supported by the observation of a relatively small Young's modulus, E_{45}, that is nearly the same as E_v.

Especially the sandy facies were rather heterogeneous, which made it difficult to get three differently oriented core plugs with the same mechanical properties that is needed for anisotropy characterization and comparison of static, seismic, and ultrasonic data. It is therefore desirable to compare static and dynamic properties measured with a single sample. This is possible with a new technique that was developed in the course of this work, and that allows for directly measuring the uniaxial-strain (P-wave) modulus as seismic frequencies. First results obtained with core plugs from the shaly facies of Opalinus Clay are presented in this work. The systematic error of the P-wave modulus obtained by measurements is significantly lower than that obtained from Young's moduli and Poisson's-ratios from three differently oriented samples.

Acknowledgements

This work was performed on behalf of NAGRA, Switzerland. We acknowledge Dr. Silvio Giger from NAGRA for providing information on Opalinus Clay and sample preparation, as well as several helpful discussions. The authors also acknowledge support from the Joint Industry Project "Shale Rock Physics" at SINTEF Petroleum Research, funded by The Research Council of Norway through the PETROMAKS 2 Programme (Grant #: 234074) and the participating companies BP, DONG Energy, Engie, Maersk and Total. The authors would also like to acknowledge Prof. Martin Mazurek and his group at University of Berne for providing mineralogical properties of the tested samples.

The authors of this paper have no conflict of interest to declare.

List of tables

List of figures

References

Batzle, M.L., Hofmann, R., Kumar, G., Duranti, L., and Han, D. (2005). Seismic Attenuation: Observations And Mechanisms. In SEG-2005-1565, (SEG: Society of Exploration Geophysicists), p.

Batzle, M.L., Han, D.-H., and Hofmann, R. (2006). Fluid mobility and frequency-dependent seismic velocity — Direct measurements. GEOPHYSICS *71*, N1–N9.

Bossart, P. (2011). Characteristics of the Opalinus Clay at Mont Terri.

Bower, A.F. (2010). Applied mechanics of solids (Boca Raton: CRC Press).

Delle Piane, C., Sarout, J., Madonna, C., Saenger, E.H., Dewhurst, D.N., and Raven, M. (2014). Frequency-dependent seismic attenuation in shales: experimental results and theoretical analysis. Geophys J Int *198*, 504–515.

Detournay, E., and Cheng, A.H.D. (1993). Fundamentals of poroelasticity. In Hudson, J.T. (Ed.), Comprehensive Rock Engineering, (Pergamon Press, Oxford), pp. 113–171.

Duranti, L., Ewy, R., and Hofmann, R. (2005). Dispersive and attenuative nature of shales: multiscale and multifrequency observations. In 75th Annual International Meeting, (Society of Exploration Geophysicists), pp. 1577–1580.

Eissa, E.A., and Kazi, A. (1988). Relation between static and dynamic Young's moduli of rocks. In International Journal of Rock Mechanics and Mining Sciences & Geomechanics Abstracts, (Elsevier), pp. 479–482.

Ewy, R.T. (2015). Shale/claystone response to air and liquid exposure, and implications for handling, sampling and testing. International Journal of Rock Mechanics and Mining Sciences *80*, 388–401.

Fjær, E. (2009). Static and dynamic moduli of a weak sandstone. GEOPHYSICS *74*, WA103–WA112.

Fjær, E., Holt, R.M., Horsrud, P., Raaen, A.M., and Risnes, R. (2008). Petroleum Related Rock Mechanics (Elsevier).

Fjær, E., Holt, R.M., Nes, O.M., Stenebraten, J.F., and others (2011). The transition from elastic to non-elastic behavior. In 45th US Rock Mechanics/Geomechanics Symposium, (American Rock Mechanics Association), p.

Fjær, E., Stroisz, A.M., and Holt, R.M. (2012). Combining static and dynamic measurements for evaluation of elastic dispersion. In 46th US Rock Mechanics/Geomechanics Symposium, (American Rock Mechanics Association), p.

Fjær, E., Stroisz, A.M., and Holt, R.M. (2013). Elastic Dispersion Derived from a Combination of Static and Dynamic Measurements. Rock Mechanics and Rock Engineering *46*, 611–618.

Giger, S. (2016). Personal communication.

Heerden, W.L. b (1987). General relations between static and dynamic moduli of rocks. In International Journal of Rock Mechanics and Mining Sciences & Geomechanics Abstracts, (Elsevier), pp. 381–385.

Hofmann, R. (2006). Frequency dependent elastic and anelastic properties of clastic rocks.

Holt, R. (2016). Bounds of elastic parameters characterizing transversely isotropic media: Application to shales. GEOPHYSICS *81*, C243–C252.

Holt, R.M., Nes, O.-M., Stenebraten, J.F., and Fjær, E. (2012). Static vs. dynamic behavior of shale. In 46th US Rock Mechanics/Geomechanics Symposium, (American Rock Mechanics Association), p.

Holt, R.M., Bauer, A., and Bakk, A. (2017). Overburden pore-pressure changes and their influence on 4D seismic. In SEG Technical Program Expanded Abstracts 2017, (Society of Exploration Geophysicists), pp. 3632–3636.

King, M.S. (1969). Static and dynamic elastic moduli of rocks under pressure. pp. 329–351.

Lozovyi, S., Sirevaag, T., Szewczyk, D., Bauer, A., and Fjær, E. (2017). Non-Elastic Effects in Static and Dynamic Rock Stiffness. In Proceedings of the 51th US Rock Mechanics Symposium - ARMA, (American Rock Mechanics Association), p.

Lozovyi, S., Bauer, A., Giger, S., and Chakraborty, S. (2018). Static vs. dynamic stiffness of shales: frequency and stress effects. In Proceedings of the 52th US Rock Mechanics / Geomechanics Symposium - ARMA, (American Rock Mechanics Association), p.

Lozovyi S., and Bauer A. (Manuscript in preparation). A new laboratory technique for measuring P-wave modulus at seismic frequencies to study velocity dispersion.Mavko, G., Mukerji, T., and Dvorkin, J. (2009). The rock physics handbook. Tools for seismic analysis of porous media (Cambridge, UK ; New York: Cambridge University Press).

Mikhaltsevitch, V., Lebedev, M., and Gurevich, B. (2014). Measurements of the elastic and anelastic properties of sandstone flooded with supercritical CO2. Geophysical Prospecting *62*, 1266–1277.

Minardi, A., Crisci, E., Ferrari, A., and Laloui, L. (2017). The Role of Anisotropy on the Volumetric Behaviour of Opalinus Clay upon Suction Change. In Advances in Laboratory Testing and Modelling of Soils and Shales (ATMSS), (Springer, Cham), pp. 315–321.

Müller, T.M., Gurevich, B., and Lebedev, M. (2010). Seismic wave attenuation and dispersion resulting from wave-induced flow in porous rocks — A review. GEOPHYSICS *75*, 75A147-75A164.

Nagra (2002). Projekt Opalinuston: Synthese der geowissenschaftlichen.

Nye, J.F. (1984). Physical properties of crystals: their representation by tensors and matrices (Oxford [Oxfordshire] : New York: Clarendon Press ; Oxford University Press).

Pearson, F.J., and Waber, H.N. (2006). Diffusion and retention (DR) experiment: Experimental water chemistry.

Pimienta, L., Fortin, J., and Guéguen, Y. (2015). Bulk modulus dispersion and attenuation in sandstones. GEOPHYSICS *80*, D111–D127.

Sarker, R., and Batzle, M.L. (2010). Anisotropic Elastic Moduli of the Mancos B Shale- An Experimental Study. In 2010 SEG Annual Meeting, (Denver, Colorado), p.

Schuster, K., Amann, F., Yong, S., Bossart, P., and Connolly, P. (2017). High-resolution mini-seismic methods applied in the Mont Terri rock laboratory (Switzerland). Swiss Journal of Geosciences *110*, 213–231.

Skempton, A.W. (1954). The Pore-Pressure Coefficients A and B. Géotechnique *4*, 143–147.

Spencer, J.W. (1981). Stress relaxations at low frequencies in fluid-saturated rocks: Attenuation and modulus dispersion. Journal of Geophysical Research *86*, 1803–1812.

Spencer, J.W., and Shine, J. (2016). Seismic wave attenuation and modulus dispersion in sandstones. GEOPHYSICS *81*, D211–D231.

Suarez-Rivera, R., Willson, S.M., Nakagawa, S., and Magnar-Ness, O. (2001). Frequency Scaling for Evaluation of Shale and Mudstone Properties from Acoustic Velocities. AGU Fall Meeting Abstracts *32*.

Subramaniyan, S., Quintal, B., Tisato, N., Saenger, E.H., and Madonna, C. (2014). An overview of laboratory apparatuses to measure seismic attenuation in reservoir rocks: Apparatuses to measure seismic attenuation. Geophysical Prospecting *62*, 1211–1223.

Szewczyk, D., Bauer, A., and Holt, R.M. (2016). A new laboratory apparatus for the measurement of seismic dispersion under deviatoric stress conditions. Geophysical Prospecting *64*, 789–798.

Szewczyk, D., Holt, R.M., and Bauer, A. (2018). The impact of saturation on seismic dispersion in shales — Laboratory measurements. GEOPHYSICS *83*, MR15–MR34.

Thomsen, L. (1986). Weak elastic anisotropy. GEOPHYSICS *51*, 1954–1966.

Tisato, N., and Madonna, C. (2012). Attenuation at low seismic frequencies in partially saturated rocks: Measurements and description of a new apparatus. Journal of Applied Geophysics *86*, 44–53.

Tutuncu, A.N. (2010). Anisotropy, Compaction And Dispersion Characteristics of Reservoir And Seal Shales. In 44th U.S. Rock Mechanics Symposium and 5th U.S.-Canada Rock Mechanics Symposium, 27-30 June, Salt Lake City, Utah, p.

Tutuncu, A.N., Podio, A.L., Gregory, A.R., and Sharma, M.M. (1998). Nonlinear viscoelastic behavior of sedimentary rocks, Part I: Effect of frequency and strain amplitude. GEOPHYSICS *63*, 184–194.

Walsh, J.B. (1966). Seismic wave attenuation in rock due to friction. Journal of Geophysical Research *71*, 2591–2599.

Wang, H.F. (2000). Theory of Linear Poroelasticity with Applications to Geomechanics and Hydrogeology (Princeton University Press).

Winkler, K., Nur, A., and Gladwin, M. (1979). Friction and seismic attenuation in rocks. Nature *277*, 528–531.

Yale, D.P., and Swami, V. (2017). Conversion of Dynamic Mechanical Property Calculations to Static Values for Geomechanical Modeling. In 51st US Rock Mechanics/Geomechanics Symposium, (American Rock Mechanics Association), p.

Tables

Table 1: Mineralogical composition of shaly and sandy facies samples of Opalinus clay from Mont Terri underground laboratory used in this study.

	Sample #	Calcite [wt.%]	Quartz [wt.%]	Others [wt.%]	Clay minerals [wt.%]
Sandy facies	1-0	17	38	12	33
	1-45	33	34	9	24
	1-90	12	37	16	34
	2-0	8	33	11	48
	2-45	8	47	12	33
	2-90	8	36	11	45
Shaly facies	3-0	5	22	8	65
	3-45	5	21	7	66
	3-90	5	21	8	66
	4-0	5	19	7	68
	4-45	6	22	8	64
	4-90	5	19	8	68

Table 2. Sandy facies, sample 2-90: Dynamic Young's modulus and Poisson's ratio measured at the end of the consolidation period for different axial-strain creep rates.

Low-frequency measurement	Time from start of the test [h]	Average axial strain rate over 3 hours [µstrain/h]	Average Young's modulus (1-144 Hz) [GPa]	Average Poisson's ratio (1-144 Hz) [-]	Relative error (Young's modulus) to the last measurement [%]
#1	16.8	19.3	6.00	0.407	2.5
#2	22.3	1.5	6.07	0.406	1.4
#3	39	0.4	6.13	0.406	0.5
#4	43.6	0.4	6.13	0.406	0.3
#5	65.4	0.25	6.15	0.405	0.0

Table 3. Shaly facies, sample 4-90: Dynamic Young's modulus and Poisson's ratio measured at the end of the consolidation period for different axial-strain creep rates.

Low frequency measurement	Time from start of the test [h]	Average axial strain rate over 2 hours [µstrain/h]	Average Young's modulus (1-144 Hz) [GPa]	Average Poisson's ratio (1-144 Hz) [-]	Relative error (Young's modulus) to the last measurement [%]
#1	73.8	50	5.16	0.364	0.4
#2	90	10	5.18	0.363	0.2
#3	96	8	5.17	0.364	0.3
#4	112	2.5	5.19	0.364	0.0

Table 4. Skempton parameters for 12 tested samples at two stress states.

	Sample	P_{conf} = 7 MPa (P_{conf}' = 4 MPa)		P_{conf} = 13 MPa (P_{conf}' = 10 MPa)	
		Skempton B	Skempton A	Skempton B	Skempton A
Sandy facies	1-0	0.897	0.154	0.770	0.239
	1-45	0.915	0.229	0.729	0.339
	1-90	0.870	0.401	0.922	0.440
	2-0	0.895	0.167		
	2-45	0.883	0.293		
	2-90	0.860	0.452		
Shaly facies	3-0	0.905	0.129	0.819	0.153
	3-45	0.917	0.364	0.827	0.409
	3-90	0.890	0.540	0.823	0.598
	4-0	0.893	0.122		
	4-45	0.889	0.339		
	4-90	0.898	0.581		

Table 5. Static undrained stiffness parameters obtained for differently oriented samples from unloading sequences of loading/unloading cycles starting from the lower stress state (p_{conf} = 7 MPa, p_f = 3 MPa). The stress amplitude of the cycles was 4 MPa for the first set of tests (1-0, 1-45, 1-90) and 1 MPa for the other sets. The stiffnesses measured with the three samples from set #1 were not consistent, which is attributed to rock heterogeneity. For this set, the obtained stiffness-matrix parameters are not reliable (numbers in light grey).

Facies	p_{conf} [MPa]	Sample	K [GPa]	E [GPa]	ν [-]	C_{11} [GPa]	C_{33} [GPa]	C_{13} [GPa]	C_{44} [GPa]	C_{66} [GPa]
Sandy	7	1-0	11.23	9.61						
		1-45	19.89	9.10						
		1-90	12.73	2.71	0.489	-55.47	14.93	12.48	3.05	-68.23
Sandy	7	2-0	12.22	6.80						
		2-45	8.62	5.31						
		2-90	15.15	4.41	0.499	18.63	20.03	15.39	1.64	3.47
Shaly	7	3-0	11.05	7.18		19.04	13.61	12.68	0.96	3.31
		3-45	11.89	3.24						
		3-90	13.39	3.39	0.403					
Shaly	7	4-0	11.17	6.25						
		4-45	13.18	3.78						
		4-90	12.51	3.59	0.390	17.52	12.74	11.74	1.20	2.47

Table 6. Static undrained stiffness parameters obtained differently oriented samples from unloading sequences of loading/unloading cycles starting from the higher stress state (p_{conf} = 13 MPa, p_f = 3 MPa). The stress amplitude of the cycles was 4 MPa for the first set of tests (1-0, 1-45, 1-90) and 1

MPa for the third set (3-0, 3-45, 3-90). The stiffnesses measured with the three samples from set #1 were not consistent, which is attributed to rock heterogeneity. For this set, the obtained stiffness-matrix parameters are not reliable (numbers in light grey).

Facies	p_{conf} [MPa]	Sample	K [GPa]	E [GPa]	ν [-]	C_{11} [GPa]	C_{33} [GPa]	C_{13} [GPa]	C_{44} [GPa]	C_{66} [GPa]
Sandy	13	1-0	11.34	13.53						
		1-45	18.58	13.07						
		1-90	11.68	4.45	0.391	25.38	12.61	10.44	5.46	12.02
Shaly	13	3-0	10.68	9.39		18.66	12.72	10.71	1.52	4.04
		3-45	13.63	4.88						
		3-90	12.04	4.88	0.366					

Table 7. Zero stress-change limit of static undrained stiffness parameters obtained by extrapolating the incremental compliances, $d\varepsilon_{ax}/d\sigma_{ax}$ and $d\varepsilon_{rad}/d\sigma_{ax}$, during the unloading sequences to zero stress change ($\Delta\sigma_{ax} = 0$) at the lower stress state (p_{conf} = 7 MPa, p_f = 3 MPa). For set #1, the obtained stiffness-matrix parameters are probably not reliable because of rock heterogeneity (numbers in light grey).

Facies	p_{conf} [MPa]	Sample	$K_{u,0}$ [GPa]	$E_{u,0}$ [GPa]	$\nu_{u,0}$ [-]	$C_{11,0}$ [GPa]	$C_{33,0}$ [GPa]	$C_{13,0}$ [GPa]	$C_{44,0}$ [GPa]	$C_{66,0}$ [GPa]
Sandy	7	1-0	15.06	14.08						
		1-45	22.99	13.50						
		1-90	18.90	6.71	0.338	32.41	18.98	18.13	5.64	5.60
Sandy	7	2-0	17.89	10.27						
		2-45	14.75	7.22						
		2-90	15.72	5.18	0.425	22.12	17.37	14.34	2.34	5.24
Shaly	7	3-0	15.67	8.87		23.14	15.15	14.53	1.33	3.72
		3-45	16.08	4.32						
		3-90	15.08	4.28	0.374					
Shaly	7	4-0	15.75	7.78						
		4-45	16.26	4.94						
		4-90	13.55	4.08	0.359	21.41	13.57	13.22	1.64	2.99

Table 8. Zero stress-change limit of static undrained stiffness parameters obtained by extrapolating the incremental compliances, $d\varepsilon_{ax}/d\sigma_{ax}$ and $d\varepsilon_{rad}/d\sigma_{ax}$, during the unloading sequences to zero stress change ($\Delta\sigma_{ax} = 0$) at the higher stress state (p_{conf} = 13 MPa, p_f = 3 MPa). For set #1, the obtained stiffness-matrix parameters are probably not reliable because of rock heterogeneity (numbers in light grey).

Facies	p_{conf}	Sample	K_u	E_u	ν_u	C_{11}	C_{33}	C_{13}	C_{44}	C_{66}

	[MPa]		[GPa]	[GPa]	[-]	[GPa]	[GPa]	[GPa]	[GPa]	[GPa]
Sandy	13	1-0	13.99	18.66						
		1-45	-	16.89						
		1-90	16.78	10.18	0.328	28.90	19.15	13.67	6.69	8.05
Shaly	13	3-0	16.31	10.98		23.73	15.62	13.83	1.83	4.54
		3-45	19.69	5.81						
		3-90	15.17	5.66	0.360					

Table 9. Ultrasonic velocities, Thomsen anisotropy parameters, and dynamic stiffness parameters at ultrasonic frequency (500 kHz) for the lower hydrostatic stress state (p_{conf} = 7 MPa, p_f = 3 MPa) and the higher hydrostatic stress state (p_{conf} = 13 MPa, p_f = 3 MPa).

Facies	p_{conf} [MPa]	Sample	V_P [m/s]	V_S [m/s]	ε [-]	γ [-]	δ [-]	C_{11} [GPa]	C_{33} [GPa]	C_{13} [GPa]	C_{44} [GPa]	C_{66} [GPa]
Sandy	7	1-0	3707		0.16			34.59	26.29			
		1-45	3998									
		1-90	3232									
	13	1-0	3800		0.15			36.34	28.15			
		1-45	4075									
		1-90	3344									
Sandy	7	2-0	3420		0.16			28.89	21.97			
		2-45	3335									
		2-90	2982									
Shaly	7	3-0	3293	1729	0.25	0.85	-0.01	26.61	17.67	8.20	2.71	7.33
		3-45	2867									
		3-90	2683	1051								
	13	3-0	3417		0.26		0.01	28.65	18.96	9.41	2.82	
		3-45	2984									
		3-90	2780	1072								
Shaly	7	4-0	3243	1706	0.25	0.72	0.15	25.80	17.18	9.70	2.92	7.14
		4-45	2911									
		4-90	2646	1091								

Figures

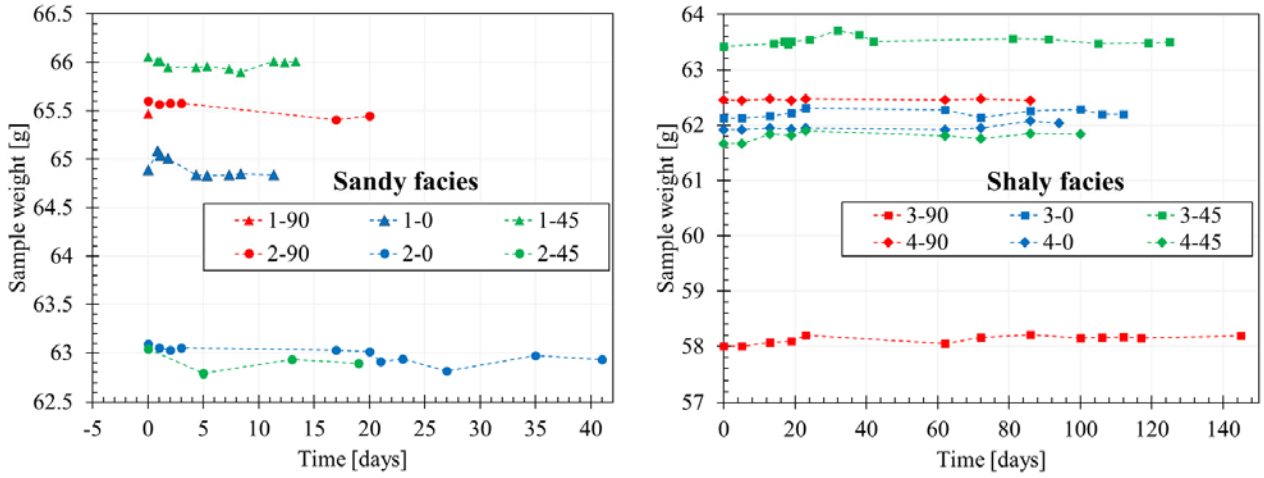

Figure 1: Weight of the core plugs as a function of time during their time in the desiccators.

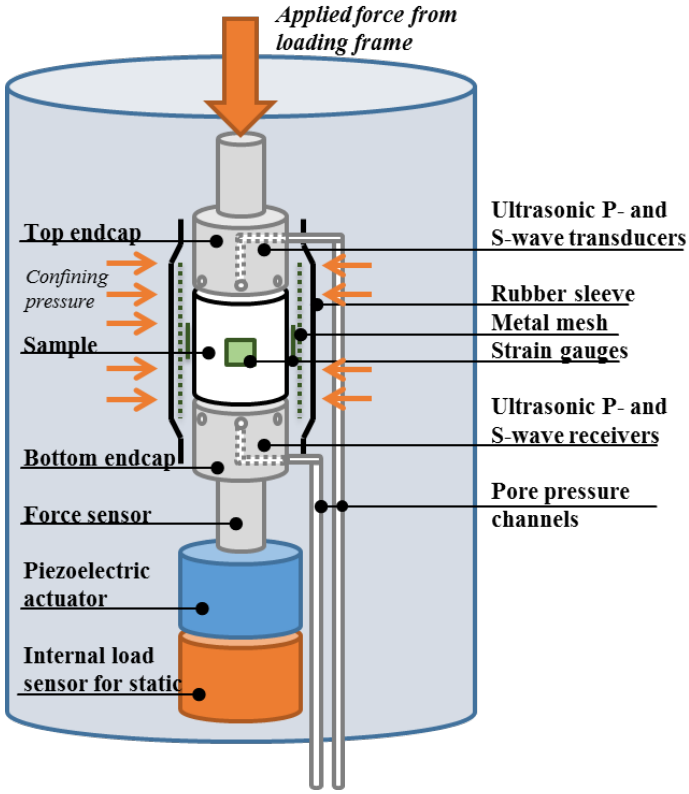

Figure 2: Schematic sketch of SINTEF's low-frequency cell.

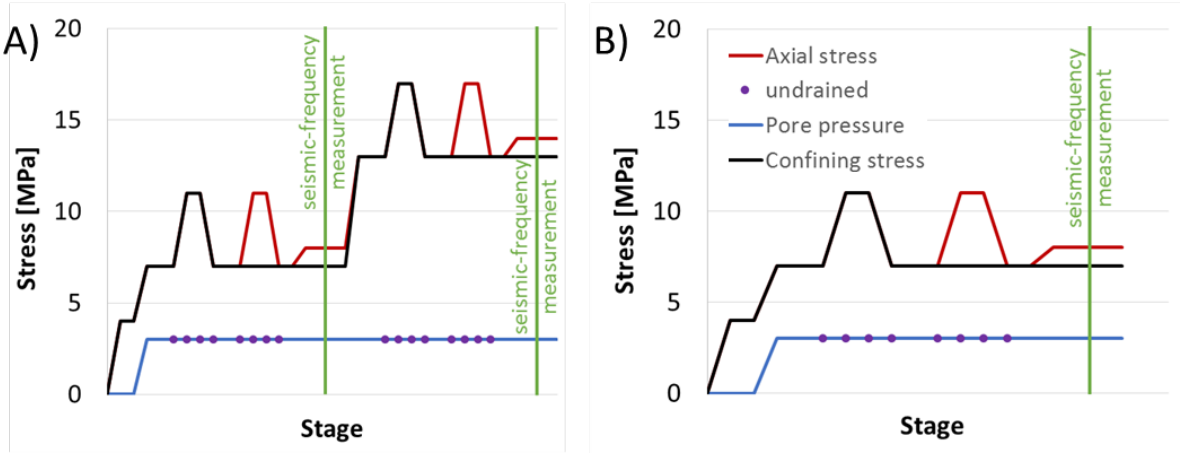

Figure 3. Test protocols: A) Main tests (set #1 and #3); B) Repeat tests (set #2 and #4). The time per stage varies significantly, depending on consolidations times. A low-frequency measurement takes approximately one hour. The dotted parts of the pore-pressure curve indicate undrained sequences during which the pore-fluid was shut in (the pore pressure generally changes during the undrained stress cycles, which is not shown here).

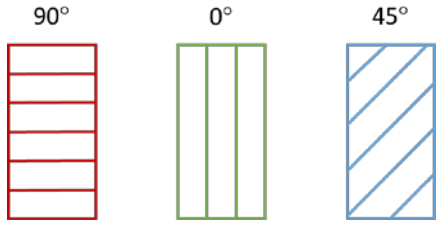

Figure 4: Sample orientations used in the present project. The parallels indicate bedding planes.

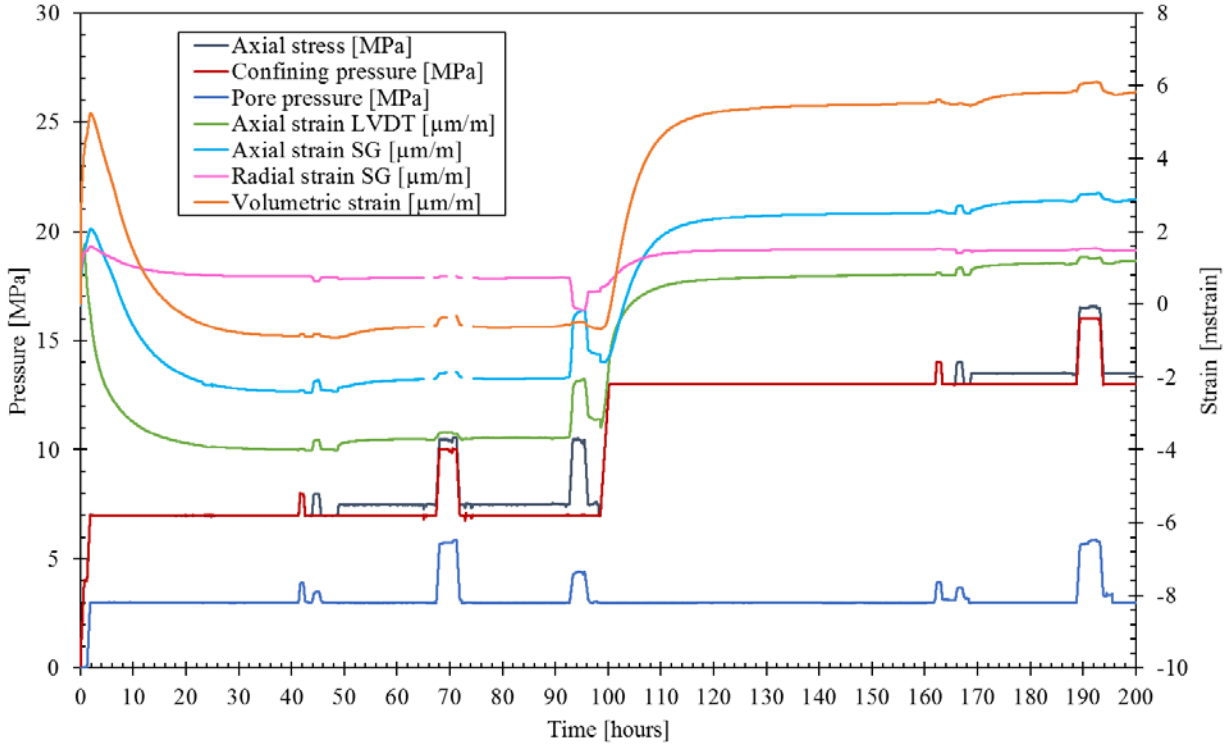

Figure 5. Stresses and strains as a function of time for the test with sample #3-90 (shaly facies). Note the swelling of the sample (negative strains) after the sample was brought in contact with brine over the first 30 hours, and the compaction after around 100 hours when the sample is brought to the higher stress state. For this test, some additional loading/unloading cycles were added outside of the scope of this paper.

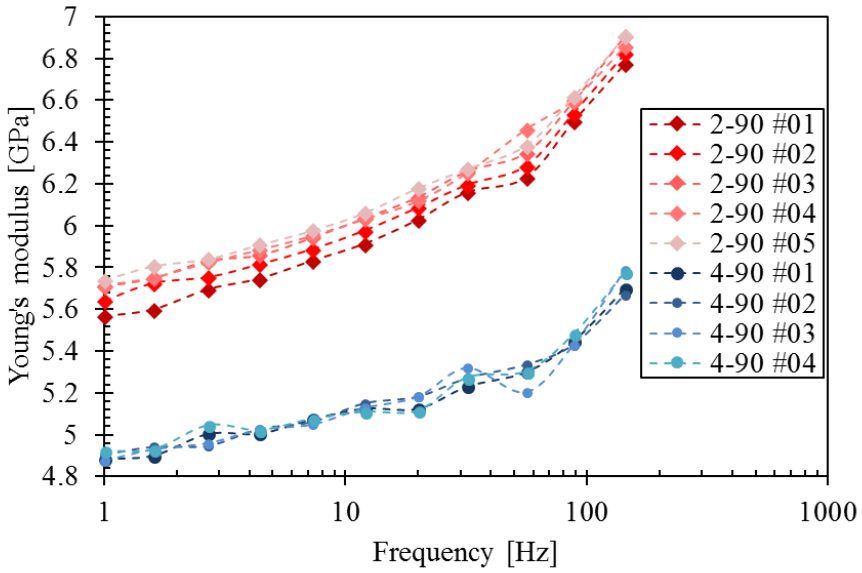

Figure 6**. Sample 2-90 (sandy facies) and Sample 4-90 (shaly facies): Dynamic Young modulus as a function of frequency at the end of the consolidation period for different axial-strain creep rates (see Table 2 and Table 3).**

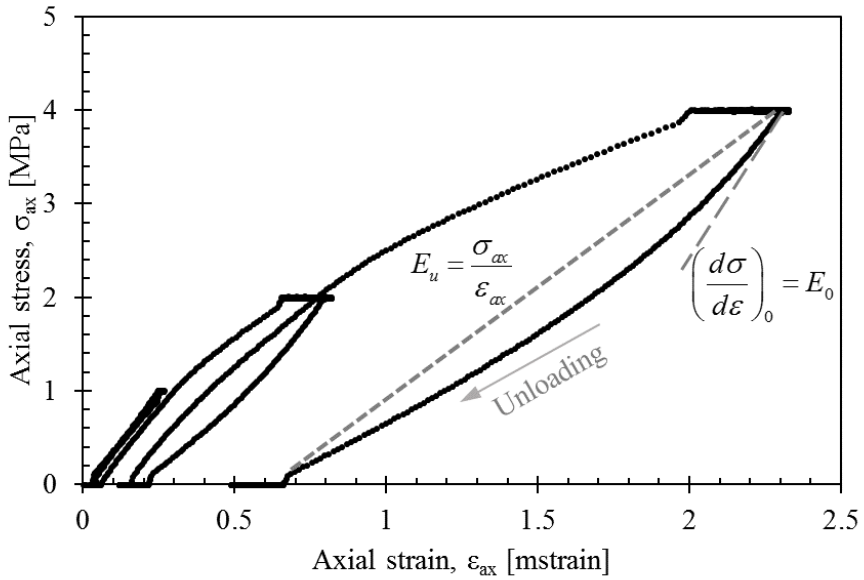

Figure 7. Stress-strain curves recorded with sample #2-90 for three subsequent undrained triaxial loading/unloading cycles with 1 MPa, 2 MPa, and 4 MPa stress amplitudes. Prior to each stress cycles, the sample was stabilized (drained conditions) at p_{conf} = 7 MPa, and p_f = 3 MPa.

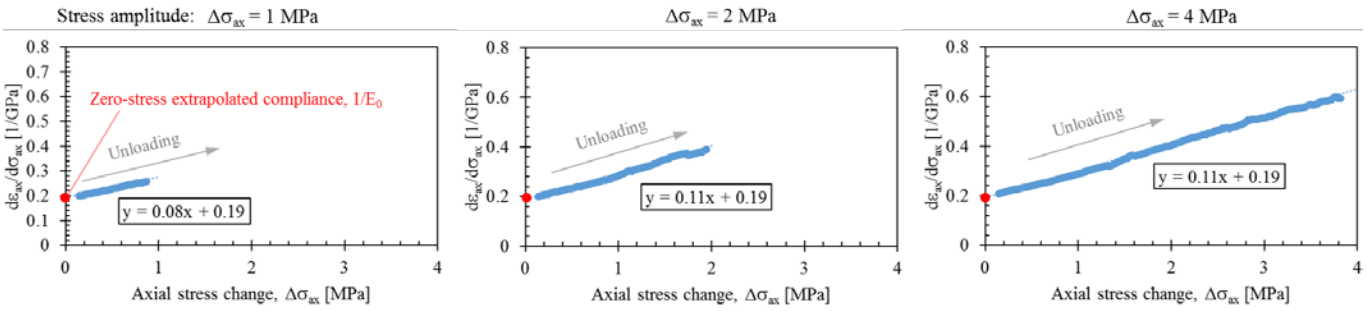

Figure 8. Incremental compliance, $d\varepsilon_{ax}/d\sigma_{ax}$, as a function of stress change, $\Delta\sigma_{ax}$, during the unloading sequences of the undrained triaxial loading/unloading cycles performed with sample #2-90.

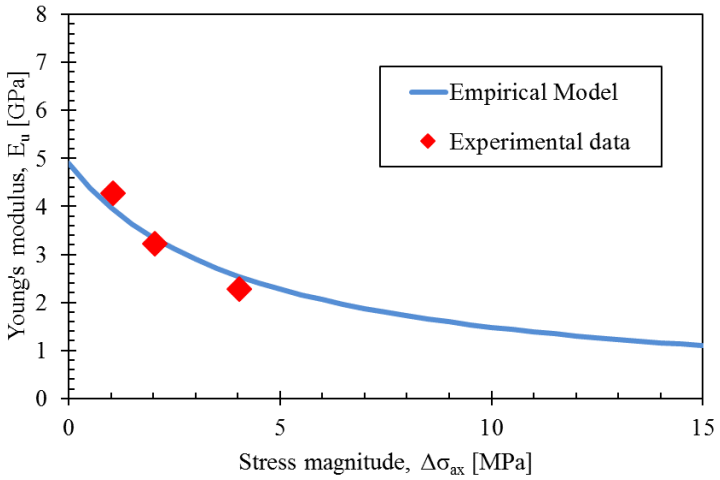

Figure 9. Average undrained Young modulus, $E_u = \Delta\sigma_{ax}/\Delta\varepsilon_{ax}$, as a function of stress change (symbols) obtained from the unloading sequences of undrained triaxial loading/unloading cycles with different stress amplitude performed with sample #2-90. The solid line represents a fit curve following Eq. 11.

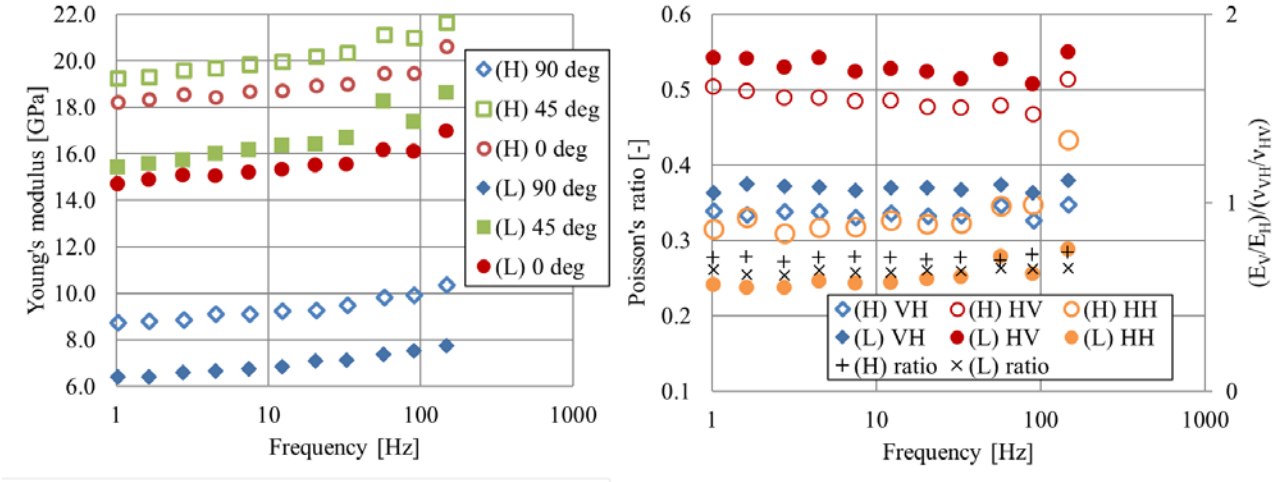

Figure 10. Sandy facies, set #1: Dynamic Young's moduli and Poisson's ratios measured with the 0°, 45° and 90° samples at the lower stress state ((L): p_{conf} = 7 MPa, σ_{ax} = 8 MPa, p_f = 3 MPa) and at the higher stress state ((H): p_{conf} = 13 MPa, σ_{ax} = 11 MPa, p_f = 3 MPa). The ratio of the ratios of Young's moduli and Poisson's ratios are plotted to the right.

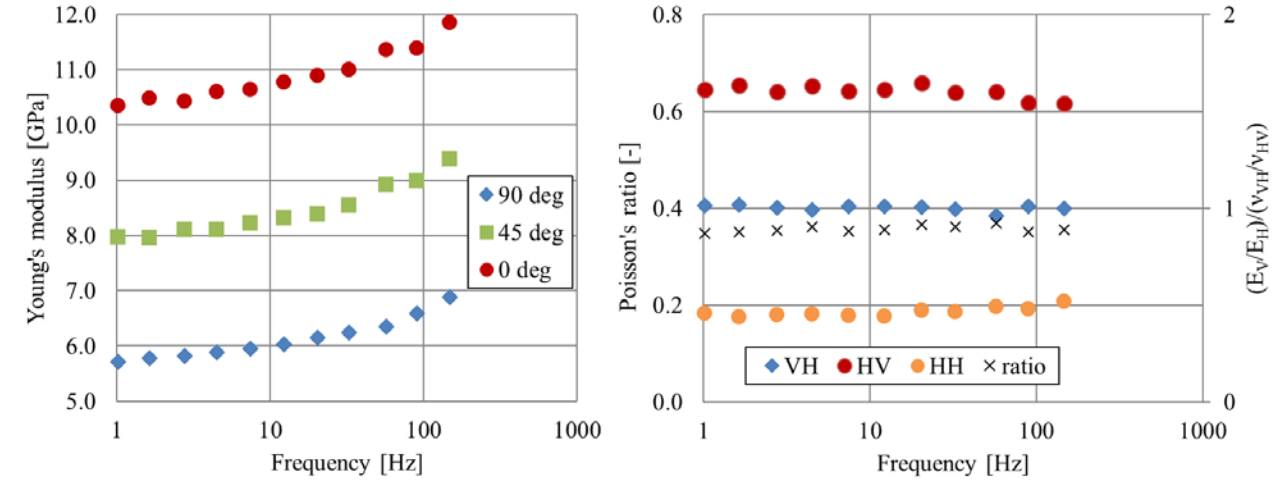

Figure 11. Sandy facies, set #2: Dynamic Young's moduli and Poisson's ratios measured with the 0°, 45° and 90° samples at the lower stress state (p_{conf} = 7 MPa, σ_{ax} = 8 MPa, p_f = 3 MPa). The ratio of the ratios of Young's moduli and Poisson's ratios are plotted to the right.

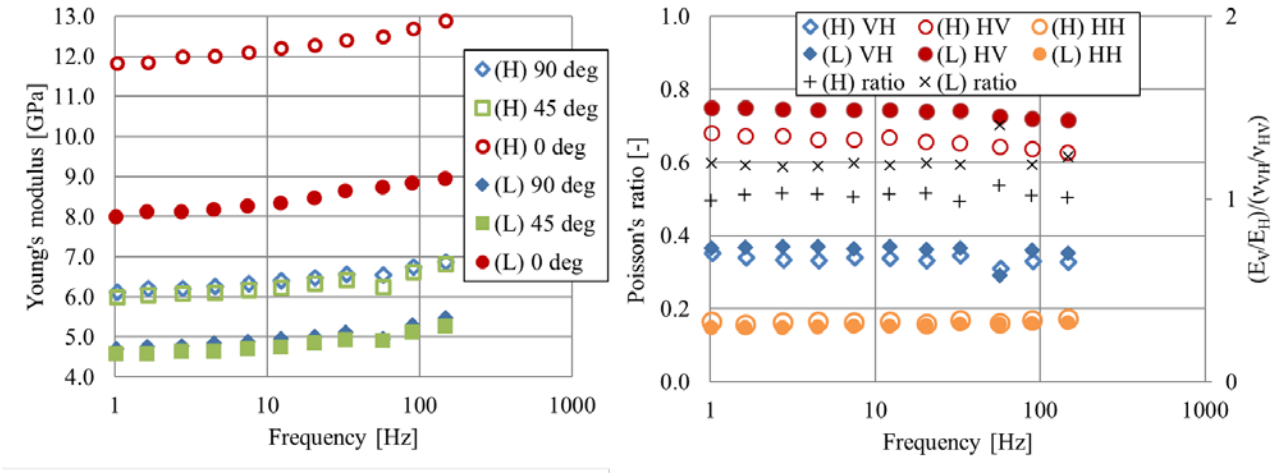

Figure 12**. Shaly facies, set #3: Dynamic Young's moduli and Poisson's ratios measured with the 0°, 45° and 90° samples at the lower stress state ((L): p_{conf} = 7 MPa, σ_{ax} = 8 MPa, p_f = 3 MPa) and at the higher stress state ((H): p_{conf} = 13 MPa, σ_{ax} = 11 MPa, p_f = 3 MPa).The ratio of the ratios of Young's moduli and Poisson's ratios are plotted to the right.**

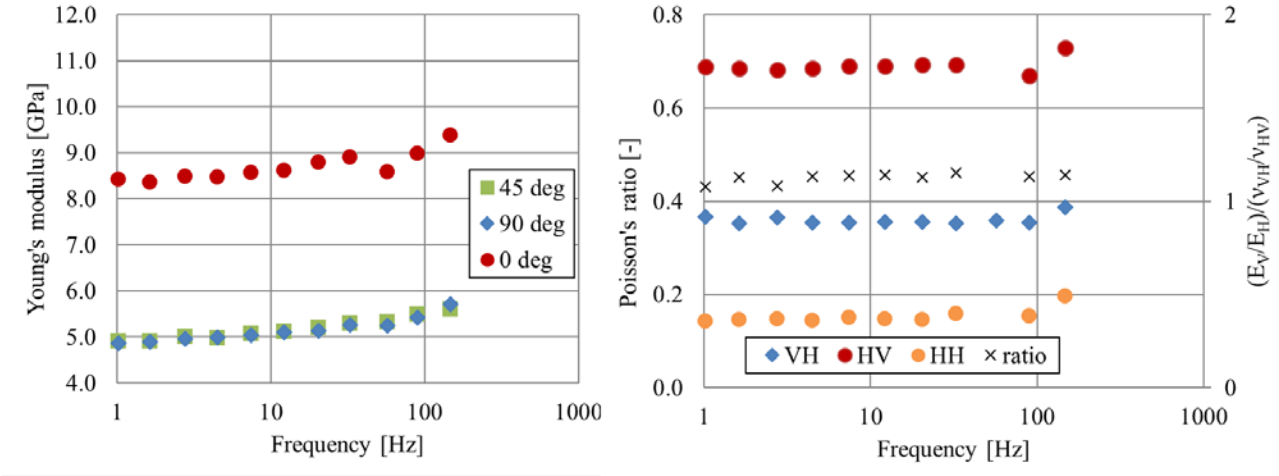

Figure 13**. Shaly facies, set #4: Dynamic Young's moduli and Poisson's ratios measured with the 0°, 45° and 90° samples at the lower stress state (p_{conf} = 7 MPa, σ_{ax} = 8 MPa, p_f = 3 MPa). The ratio of the ratios of Young's moduli and Poisson's ratios are plotted to the right.**

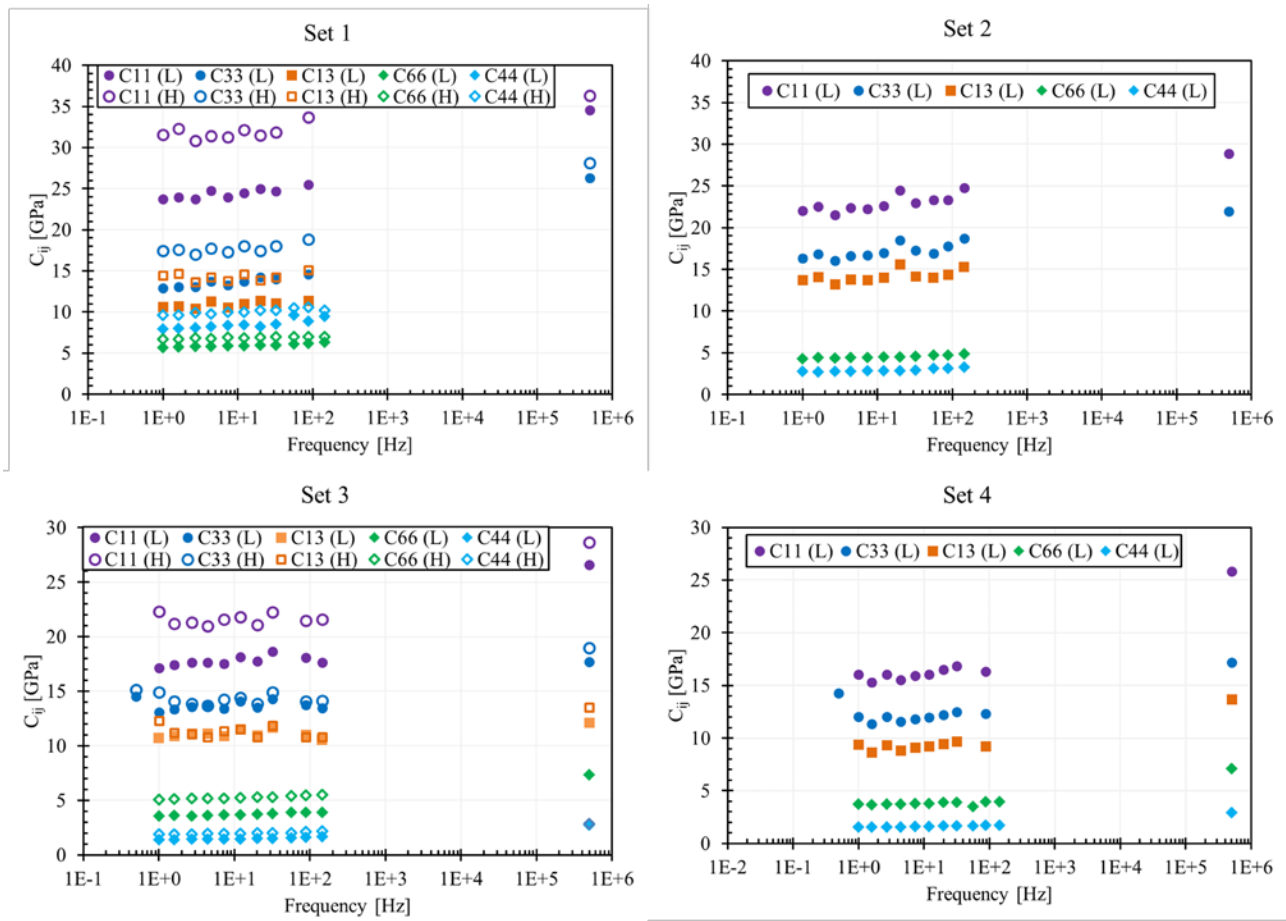

Figure 14**. Stiffness-matrix elements C_{ij} shown as functions of frequency for four tested sets of samples (sandy facies: #1 and #2; shaly facies: #3 and #4) and two stress states (closed symbols - lower stress state (L): p_{conf} = 7 MPa, σ_{ax} = 8 MPa, p_f = 3 MPa and open symbols - higher stress state (H): p_{conf} = 13 MPa, σ_{ax} = 11 MPa, p_f = 3 MPa).**

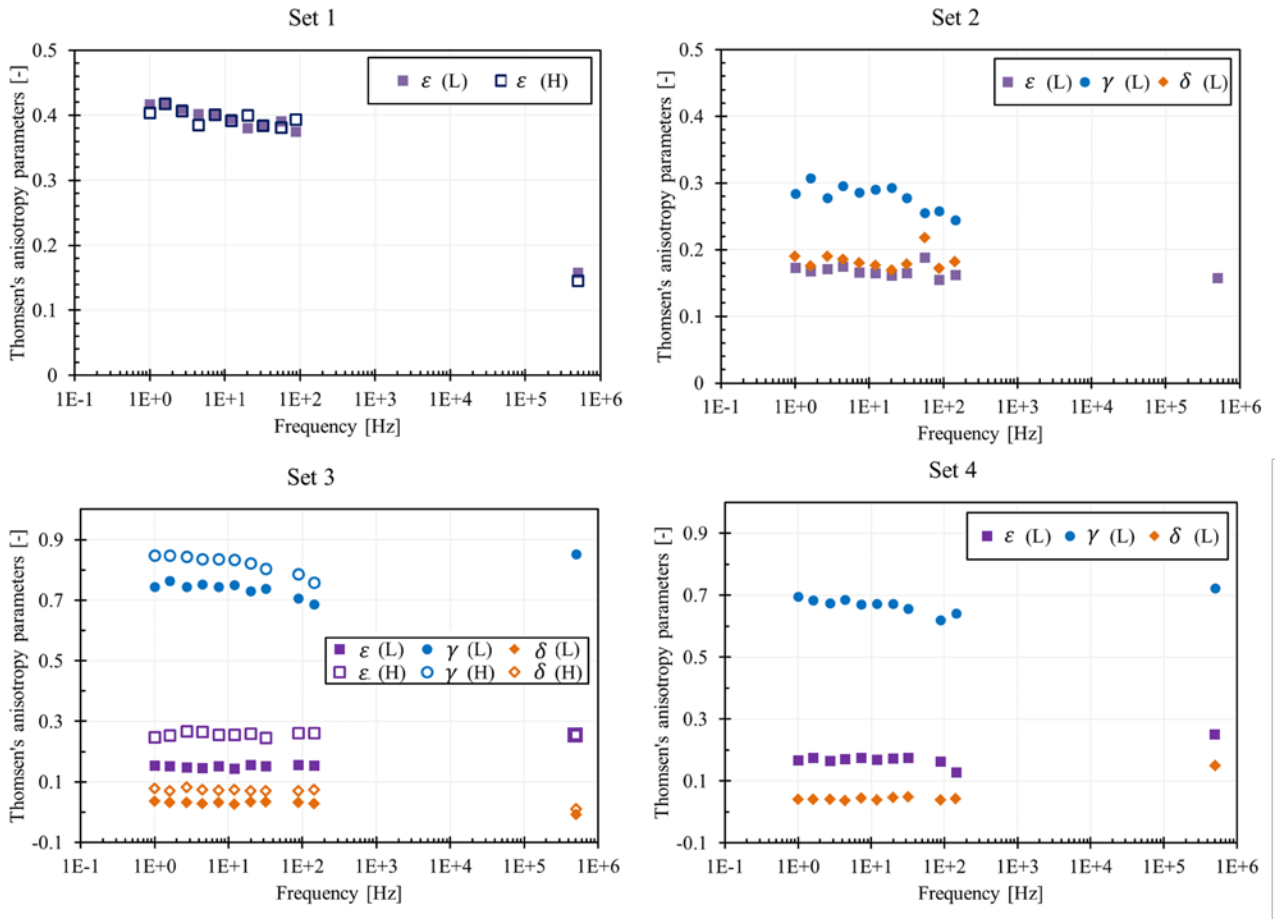

Figure **15**. Thomsen anisotropy parameters ε, γ, δ shown as functions of frequency for four tested sets of samples (sandy facies: #1 and #2; shaly facies: #3 and #4) and two stress states (closed symbols - lower stress state (L): p_{conf} = 7 MPa, σ_{ax} = 8 MPa, p_f = 3 MPa and open symbols - higher stress state (H): p_{conf} = 13 MPa, σ_{ax} = 11 MPa, p_f = 3 MPa).

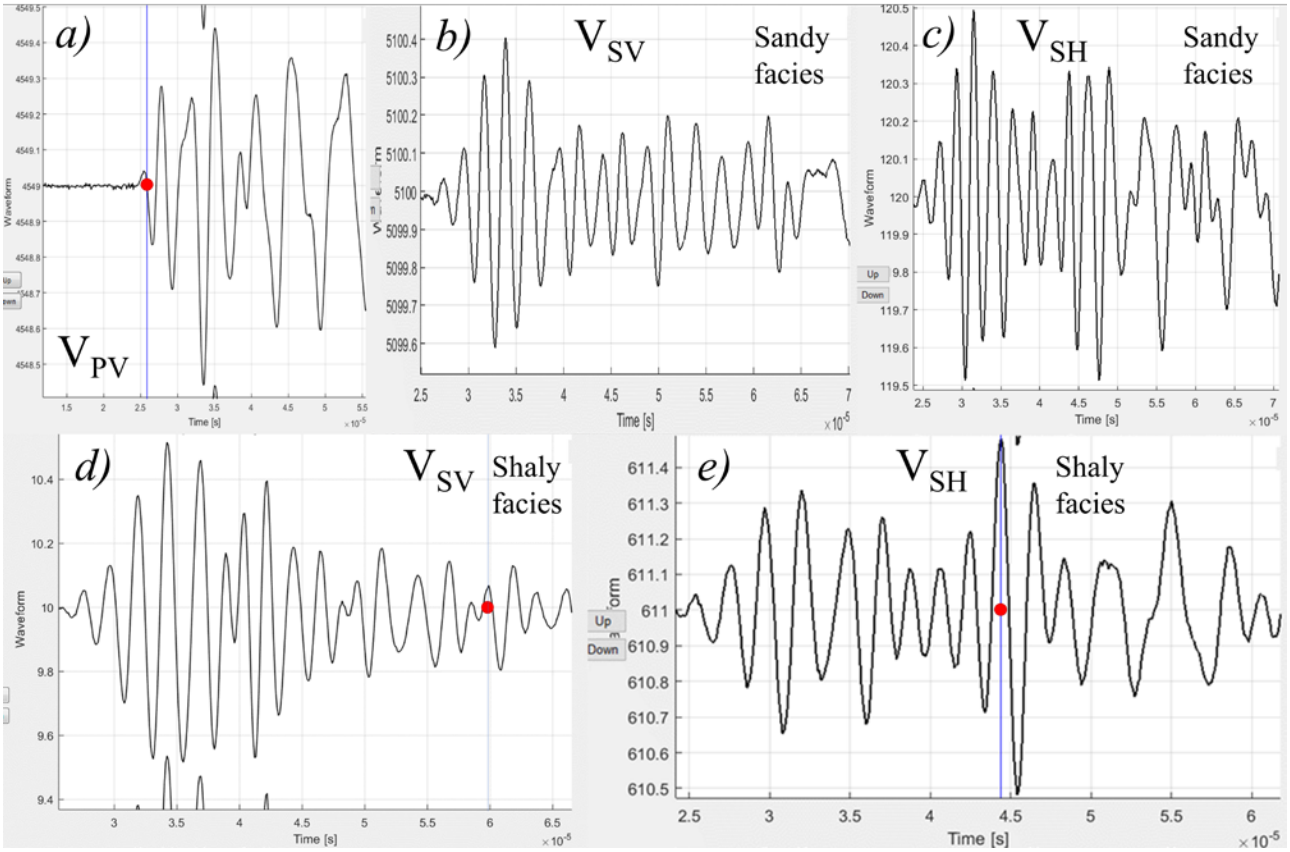

Figure 16. Typical pulse-transmission waveforms of a P-wave (a) and S-waves (b-e). Picking of the S-wave arrival was in some cases not possible or challenging because of the large p-converted signal before the S-wave arrival (see waveforms b-e). Only for shaly facies picking of the S-wave arrival was possible (waveforms d and e). The waveforms shown here were measured with sample 2-90 (a and b, the polarization of the S-wave was perpendicular to bedding), sample 2-0 (c, the polarization of the S-wave was parallel to bedding), 3-90 (d, the polarization of the S-wave was perpendicular to bedding), sample 3-0 (e, the polarization of the S-wave was parallel to bedding).

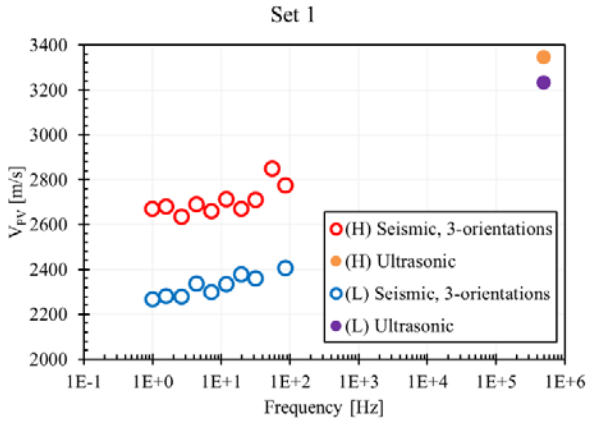

Figure 17**. Sandy facies, set #1: Dispersion of V_{PV} (left) for the lower (L) and the higher (H) stress state. There is no data available for S-wave velocities, neither for seismic frequencies (the data from the 45° test that is needed to calculate V_{SV} was not consistent), nor for ultrasonic frequencies.**

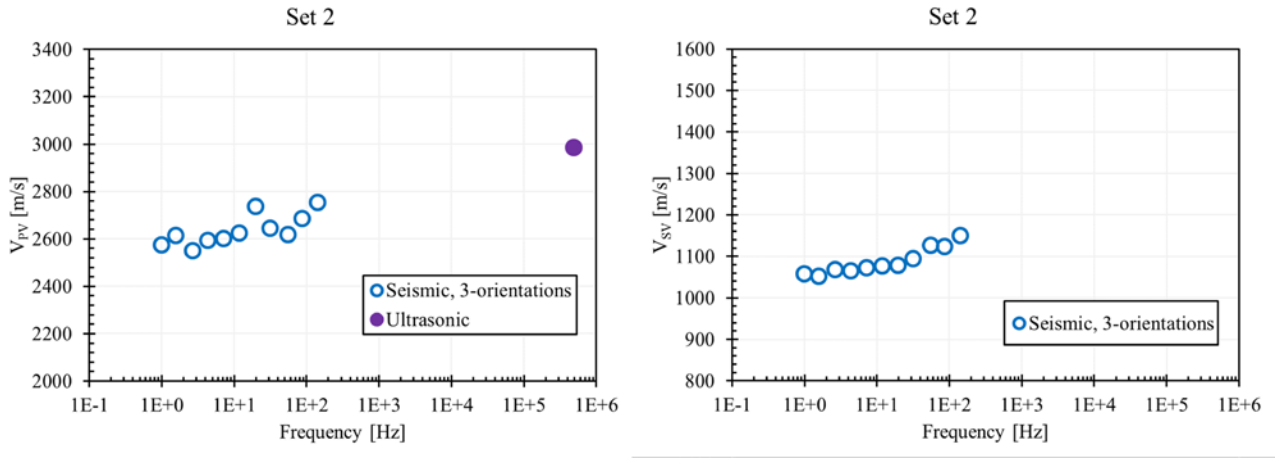

Figure 18**. Sandy facies, set #2: Dispersion of V_{PV} (left) and V_{SV} (right) for the sandy facies for the lower stress state. There is no data available for the ultrasonic V_{SV}.**

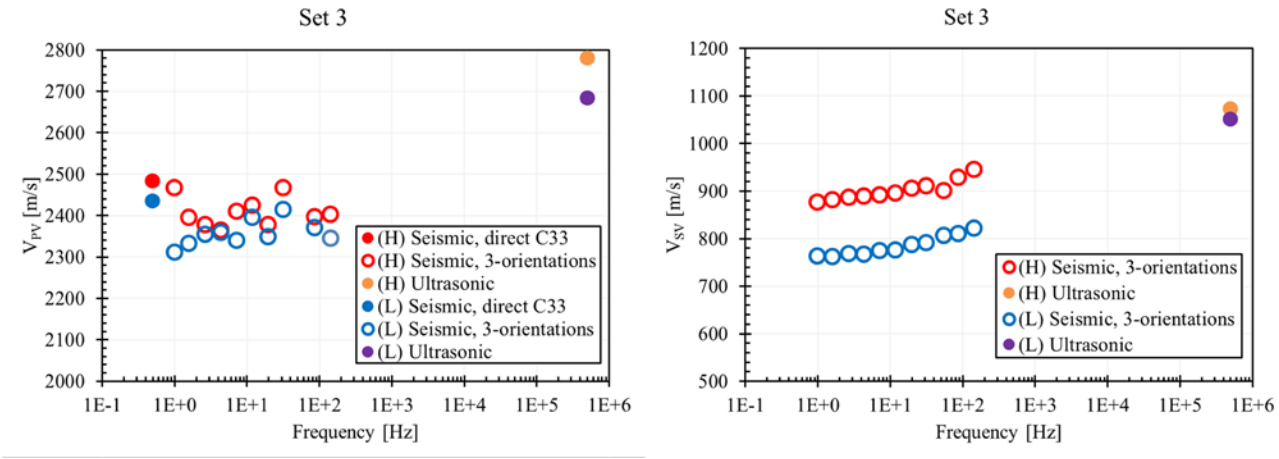

Figure 19**. Shaly facies, set #3: Dispersion of V_{PV} (left) and V_{SV} (right) for the lower and the higher stress state.**

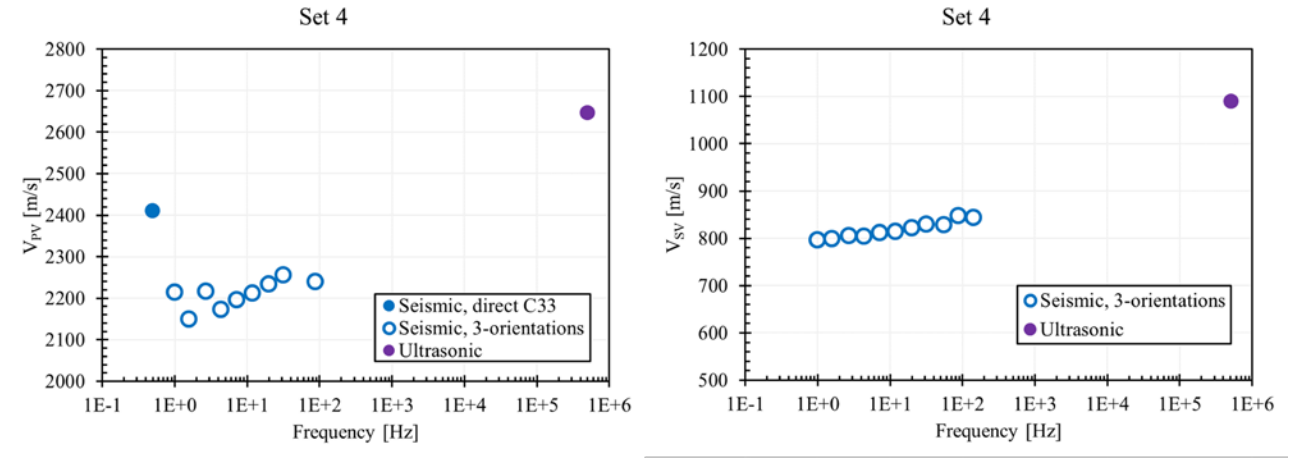

Figure 20**. Shaly facies, set #4: Dispersion of V_{PV} (left) and V_{SV} (right) for the lower stress state.**

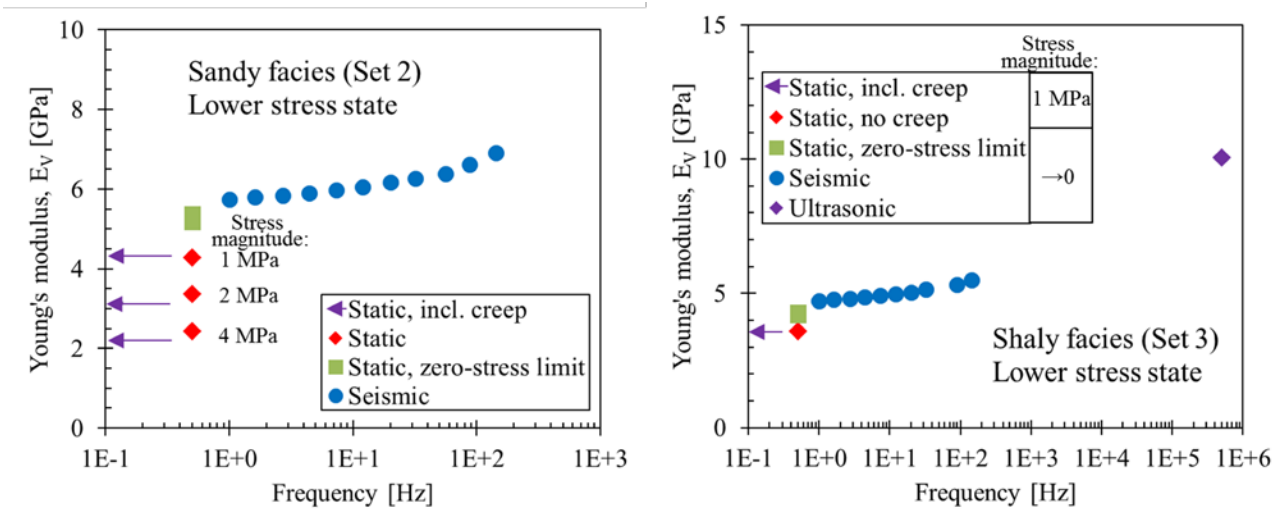

Figure 21**. Quasi-static (red symbols), zero-stress extrapolated quasi-static (green symbols), and dynamic Young modulus (blue and purple symbols) as a function of frequency for sample 2-90 (sandy facies, left), and for sample 3-90 (shaly facies, right). The static Young moduli (zero-frequency limit, including creep effects) are indicated by the arrows.**